

FATIGUE BEHAVIOR OF WELDED API 5L X70 PIPELINE STEEL

A THESIS SUBMITTED TO  
THE GRADUATE SCHOOL OF NATURAL AND APPLIED SCIENCES  
OF  
MIDDLE EAST TECHNICAL UNIVERSITY

BY

ŞERMİN ÖZLEM TURHAN

IN PARTIAL FULFILLMENT OF THE REQUIREMENTS  
FOR  
THE DEGREE OF MASTER OF SCIENCE  
IN  
METALLURGICAL AND MATERIALS ENGINEERING

APRIL 2020



Approval of the thesis:

**FATIGUE BEHAVIOR OF WELDED API 5L X70 PIPELINE STEEL**

submitted by **ŞERMIN ÖZLEM TURHAN** in partial fulfillment of the requirements for the degree of **Master of Science in Metallurgical and Materials Engineering, Middle East Technical University** by,

Prof. Dr. Halil Kalıpçılar  
Dean, Graduate School of **Natural and Applied Sciences** \_\_\_\_\_

Prof. Dr. Cemil Hakan Gür  
Head of the Department, **Metallurgical and Materials Eng.** \_\_\_\_\_

Prof. Dr. Rıza Gürbüz  
Supervisor, **Metallurgical and Materials Eng., METU** \_\_\_\_\_

**Examining Committee Members:**

Prof. Dr. Bilgehan Ögel  
Metallurgical and Materials Eng., METU \_\_\_\_\_

Prof. Dr. Rıza Gürbüz  
Metallurgical and Materials Eng., METU \_\_\_\_\_

Prof. Dr. Cevdet Kaynak  
Metallurgical and Materials Eng., METU \_\_\_\_\_

Prof. Dr. Vedat Akdeniz  
Metallurgical and Materials Eng., METU \_\_\_\_\_

Assoc. Prof. Dr. Ziya Esen  
Materials Science and Eng., Çankaya Uni. \_\_\_\_\_

Date: 30.04.2020

**I hereby declare that all information in this document has been obtained and presented in accordance with academic rules and ethical conduct. I also declare that, as required by these rules and conduct, I have fully cited and referenced all material and results that are not original to this work.**

Name, Last name : Şermin Özlem, Turhan

Signature :

## ABSTRACT

### FATIGUE BEHAVIOR OF WELDED API 5L X70 PIPELINE STEEL

Turhan, Şermin Özlem  
Master of Science, Metallurgical and Materials Engineering  
Supervisor: Prof. Dr. Rıza Gürbüz

April 2020, 76 pages

In this study, fatigue failure behavior of welded X70 pipeline steel was investigated by rotating bar bending fatigue tests performed at room temperature. S-N curves of base metal, weld and heat-affected zone (HAZ) were plotted. Tension tests, hardness measurements and Charpy V notched impact tests were carried out for mechanical characterization. Microstructural examination was conducted by optical microscope and scanning electron microscope (SEM). Fracture surfaces were examined with SEM. In addition to fractographic analysis, striation spacing was used to estimate the crack growth rate of base metal, weld and HAZ. Stress intensity factor ( $\Delta K$ ) ranges were also calculated. Tensile properties and hardness values of base metal and weld were found to be almost the same. Charpy impact test results show that base material has approximately twice impact energy than weld and HAZ at room temperature. However, Charpy impact energies of HAZ and weld decreased noticeably at  $-30\text{ }^{\circ}\text{C}$  while very slight decrease was observed for base metal. The comparison of high cycle fatigue and crack growth behaviors shows that base metal has a better fatigue behavior than weld and HAZ from the point of crack initiation and propagation. Moreover, our findings also support the idea that striation spacing can be used as a fractographic approach in order to estimate the crack growth behavior of materials.

Keywords: Pipeline Steels, Fatigue, S-N Curves, X70 Steel, Striation Spacing

## ÖZ

### KAYNAKLI API 5L X70 BORU HATTI ÇELİĞİNİN YORULMA DAVRANIŞI

Turhan, Şermin Özlem  
Yüksek Lisans, Metalurji ve Malzeme Mühendisliği  
Tez Yöneticisi: Prof. Dr. Rıza Gürbüz

Nisan 2020, 76 sayfa

Bu çalışmada, kaynaklı X70 boru hattı çeliğinin yorulma davranışı, oda sıcaklığında gerçekleştirilen dönen çubuk eğme yorulma testleri ile araştırıldı. Ana metal, kaynak ve ısıdan etkilenen bölgenin S-N eğrileri çizildi. Mekanik karakterizasyon için çekme testleri, sertlik ölçümleri ve Charpy V çentikli darbe deneyleri yapıldı. Mikroyapısal inceleme optik mikroskop ve taramalı elektron mikroskobu (SEM) ile gerçekleştirildi. Kırılma yüzeyleri SEM ile incelendi. Fraktografik analize ek olarak, ana metal, kaynak ve ısıdan etkilenen bölgenin çatlak büyüme hızını tahmin etmek için yorulma izi mesafesi kullanıldı. Gerilme yoğunluk faktörü ( $\Delta K$ ) aralıkları da hesaplandı. Ana metal ve kaynağın gerilme özellikleri ve sertlik değerleri hemen hemen aynı bulundu. Charpy darbe testi sonuçları, ana malzemenin oda sıcaklığında kaynak ve ısıdan etkilenen bölgeden yaklaşık iki kat daha fazla darbe enerjisine sahip olduğunu gösterdi. Bununla birlikte, ısıdan etkilenen bölge ve kaynağın Charpy darbe enerjileri  $-30\text{ }^{\circ}\text{C}$ 'da belirgin bir şekilde azalırken, ana metal için çok hafif bir düşüş gözlemlendi. Yüksek ömürlü yorulma ve çatlak büyüme davranışlarının karşılaştırılması; ana metalin, çatlak oluşumu ve ilerlemesi açısından ana metal ve ısıdan etkilenen bölgeden daha iyi bir yorulma davranışına sahip olduğunu gösterdi. Ayrıca bulgularımız, yorulma izi mesafesinin malzemelerin çatlak büyüme

davranışını tahmin etmek için fraktografik bir yaklaşım olarak kullanılabileceği fikrini de desteklemektedir.

Anahtar Kelimeler: Boru Hattı Çelikleri, Yorulma, S-N Eğrisi, X70 Çeliđi, Yorulma İzi Mesafesi

To my beloved family

## ACKNOWLEDGMENTS

I wish to express my deepest gratitude to Cemal Yanardağ for his technical support. Without his help, I would never have finished this thesis.

I would like to thank my supervisor Prof. Dr. Rıza Gürbüz for his guidance, advice, criticism and encouragements.

I would also like to thank Murat Tolga Ertürk for his suggestions and help.

I'd like to recognize the help that I received from Ali Motemani, Serkan Yılmaz, Dr. Süha Tirkeş, Mert Balcı, Yusuf Yıldırım, Mevlüt Bağcı, Yılmaz Kalaycı, İlyas Özdoğan and Eren Faik Karaarslan.

Finally, I would like to express my gratitude to my dear friends Bengi Çiftçi, Yiğit Deniz and Ceylan Anıl for reminding me how lucky I am.

## TABLE OF CONTENTS

ABSTRACT .....	v
ÖZ.....	vii
ACKNOWLEDGMENTS .....	x
TABLE OF CONTENTS.....	xi
LIST OF TABLES.....	xiv
LIST OF FIGURES .....	xv
CHAPTERS	
1 INTRODUCTION .....	1
2 THEORY .....	5
2.1 Fatigue Phenomenon .....	5
2.2 S-N Curves.....	6
2.2.1 Basquin’s Equation.....	7
2.3 Crack Growth Rate .....	8
2.4 Pipeline Steels .....	9
2.5 Welding Process .....	11
2.5.1 The Effects of Welding on Microstructure .....	13
2.5.1.1 Coarse Grained Region .....	13
2.5.1.2 Grain Refined Region .....	14
2.5.1.3 Inter-Critical Region .....	14
2.5.1.4 Base Metal .....	15
3 LITERATURE REVIEW.....	17
3.1 Welding Based Studies .....	17

3.2	Fatigue Behavior Based Studies .....	19
4	EXPERIMENTAL PROCEDURE .....	25
4.1	Material and Production Process .....	25
4.2	Welding Process .....	25
4.3	Specimen Directions Used in Experimental Procedure .....	28
4.4	Microstructural Analysis .....	29
4.5	Mechanical Analysis .....	30
4.5.1	Tension Test .....	30
4.5.1.1	Base Metal .....	30
4.5.1.2	Weld Zone .....	31
4.5.2	Hardness Measurement .....	32
4.5.3	Charpy Impact Test .....	33
4.6	Rotating Bending Fatigue Test .....	34
4.7	Strain Gage Measurement .....	38
4.8	Fractographic Analysis .....	42
5	RESULTS AND DISCUSSION .....	43
5.1	Microstructural Analysis .....	43
5.2	Mechanical Analysis .....	47
5.2.1	Tension Test Results .....	48
5.2.1.1	Base Metal .....	48
5.2.1.2	Weld Metal .....	49
5.2.2	Hardness Measurement Results .....	50
5.2.3	Charpy Impact Test Results .....	53
5.3	Rotating Bending Fatigue Test Results .....	56

5.4	Fractographic Analysis .....	61
5.4.1	Striation Spacing .....	65
6	CONCLUSION.....	71
	REFERENCES.....	73

## LIST OF TABLES

### TABLES

Table 2.1. Stress intensity factor solution for solid cylinder [21] .....	9
Table 2.2. Chemical composition of steel grade X70M (PSL2 pipe with $t \leq 25.0$ mm) [22].....	10
Table 4.1. Chemical composition of API 5L X80 steel.....	25
Table 4.2. Welding parameters.....	27
Table 4.3. Chemical composition of weld metal.....	28
Table 4.4. Specimen directions for the experiments.....	29
Table 4.5. Stress values calculated according to the strain gage measurements and moment formulas .....	41
Table 5.1. Tensile test results of specimens from base metal region of X70 steel..	48
Table 5.2. Tensile test results of specimens prepared from weld zone of X70 steel .....	50
Table 5.3. Hardness values of base metal, heat affected zone (HAZ1, HAZ2, and HAZ3) and weld .....	51
Table 5.4. Charpy impact test results at 25 and -30 °C for BM, fusion line 1, fusion line 2, and weld.....	54
Table 5.5. Fatigue test results.....	57
Table 5.6. Macro fracture surfaces of all test groups subjected to rotating bending fatigue test .....	62
Table 5.7. Data obtained from striation counting and stress intensity factor calculations.....	69

## LIST OF FIGURES

### FIGURES

Figure 2.1. S-N curve for materials having fatigue limit .....	6
Figure 2.2. S-N curve on a log-log scale [19] .....	8
Figure 2.3. The microstructures of (a) conventional rolled steel and (b) TMCP steel [26].....	10
Figure 2.4. Schematic representation of submerged arc welding method [28].....	12
Figure 3.1. Hardness values of welded pipes; (a) without heat treatment, and (b) with heat treatment [14].....	20
Figure 3.2. S-N curves for strip specimens taken from welded pipes with and without heat treatment [14].....	20
Figure 3.3. Microhardness values of different series of X70 steel specimens; subjected to SSP, Conventionally shot peening (CSP) and not peened [8] .....	21
Figure 3.4. S-N curves for smooth specimens (a) CSP and not peened, and (b) SSP and not peened [8] .....	22
Figure 3.5. S-N curves for notched specimens (a) CSP and not peened, and (b) SSP and not peened [8] .....	22
Figure 3.6. S-N curves for X70 steel at different environments [5].....	23
Figure 3.7. S-N plot of API X52 steel at air and hydrogen environment [6].....	24
Figure 4.1. Hot rolled coil of X70 Steel.....	26
Figure 4.2. Submerged arc welding process; (a) welding, (b) cooling, (c) welded pipe .....	27
Figure 4.3. Welding groove geometry .....	28
Figure 4.4. Directions of weld and rolling .....	29
Figure 4.5. The specimen prepared for microstructure analysis in transverse direction .....	30
Figure 4.6. Tensile test specimens prepared from base metal region of X70 steel .	31
Figure 4.7. The directions of the tensile test specimens prepared from weld region of X70 steel .....	31
Figure 4.8. Tensile test specimens prepared from weld zone of X70 Steel.....	32

Figure 4.9. Lines where the hardness data were taken along; (a) upper line, (b) midline, (c) lower line .....	32
Figure 4.10. Notch locations; fusion line 1 and fusion line 2 .....	33
Figure 4.11. Charpy V-notch specimen geometry and dimensions.....	34
Figure 4.12. Rotating beam fatigue test machine .....	34
Figure 4.13. Stress vs. time graph for stress ratio (R): -1 .....	35
Figure 4.14. Geometry of hourglass type specimen and the corresponding moment (M) and stress ( $\sigma$ ) diagrams as a function of the distance (x) .....	36
Figure 4.15. Stress distribution along the smallest cross section of the specimen ..	37
Figure 4.16. Specimens with welded section .....	38
Figure 4.17. The specimen with strain gage on rotating beam fatigue test machine .....	39
Figure 4.18. Geometry of specimen prepared for strain gage analysis.....	39
Figure 4.19. Load vs. strain graph of strain gage measurements .....	40
Figure 4.20. Strain vs. time graph for the specimen loaded with 222 N .....	40
Figure 4.21. Strain gage quarter bridge showing the maximum and minimum strain values .....	40
Figure 4.22. Striation width measurement .....	42
Figure 5.1. Optical micrographs of base metal region of X70 Steel (a) Transversal cut; AF (acicular ferrite) and (b) longitudinal cut at 1000X magnification.....	43
Figure 5.2. Optical micrographs of weld region and HAZ sub-regions; (a) weld metal, (b) HAZ1, (c) HAZ2, and (d) HAZ3 at 1000X magnification .....	44
Figure 5.3. Sub-regions of HAZ in X70 steel occurred due to heating during welding process; (a) coarse grained region (HAZ1), (b) grain refined region (HAZ2), (c) inter-critical region (HAZ3), (d) base metal region.....	45
Figure 5.4. SE images from (a) base metal, (b) HAZ1, (c) HAZ2, and (d) HAZ3 of X70 Steel at 5000X and 10000X.....	47
Figure 5.5. SE images from (a) weld zone and (b) root of weld zone at 5000X.....	47
Figure 5.6. Stress – strain curves for specimens prepared from base metal region of X70 steel.....	48

Figure 5.7. Broken tensile test specimens prepared from base metal region of X70 steel.....	49
Figure 5.8. Stress – strain curves for specimens prepared from weld zone of X70 steel.....	49
Figure 5.9. Broken tensile test specimens prepared from weld zone of X70 steel .	50
Figure 5.10. Hardness profiles of lower line, midline and upper line along the base metal, HAZ and weld.....	52
Figure 5.11. Hardness profiles of midline and upper/lower line avg. along the base metal (BM), HAZ and weld .....	53
Figure 5.12. Impact specimens tested at 25 °C and the corresponding structures at the fracture surfaces; (a) base metal, (b) FL1, (c) FL2, and (d) weld metal .....	55
Figure 5.13. SEM images taken from FL2 tested at (a) 25 °C (No1), (b) - 30 °C, and (c) 25 °C (No3).....	56
Figure 5.14. S-N plot for base metal.....	58
Figure 5.15. S-N plot for weld metal.....	58
Figure 5.16. S-N plot for HAZ.....	59
Figure 5.17. S-N curves for base metal, weld and HAZ.....	60
Figure 5.18. Fatigue ratios for base metal, weld and HAZ.....	60
Figure 5.19. Basquin slopes for base metal, weld and HAZ.....	61
Figure 5.20. Fracture surface of base metal ( $\sigma = 434$ MPa); (a) ratched markings and FFZ (fast fracture zone), (b) dimples indicating rapid failure, and (c) and (d) striations indicating crack propagation direction .....	63
Figure 5.21. Fracture surface of HAZ ( $\sigma = 380$ MPa); (a) rubbed surface and FFZ (fast fracture zone), (b) tear ridge like patterns coalescing towards crack propagation direction, (c) dimples indicating rapid failure .....	64
Figure 5.22. (a) Fracture surface of welded specimen (failed at $\sigma = 379$ MPa), (b) dimples indicating rapid failure region, (c) rubbed surface, and (d) tear ridge like patterns showing the direction of crack propagation.....	65
Figure 5.23. SEM images of base metal fracture surface; (a) striation measurement point, (b) striation width measurements.....	66

Figure 5.24. SEM images of welded metal fracture surface; (a) crack initiation point, (b) striation width measurement at 3.32 mm away from crack initiation point ..... 67

Figure 5.25. SEM images of HAZ fracture surface; (a) crack initiation point, (b) striation width measurement at 3.34 mm away from crack initiation point ..... 68

Figure 5.26. Crack growth behavior of base metal, weld and HAZ..... 70

## **CHAPTER 1**

### **INTRODUCTION**

In recent years, with the increase in the production and consumption of crude oil and natural gas worldwide, the transport of materials used in energy and petrol sectors is of strategic importance [1], [2]. This has made production, installation and operation of large diameter pipes used at very long distances and under high-pressure conditions important in terms of economy and safety [3], [4]. The 70 % of energy transportation worldwide are carried out by pipelines [2]. There are also other ways of transportation on land such as trucks and trains for crude oil. However when they are compared with transportation by pipelines, it is seen that transport through the pipelines is more economical and safer [5]. The transportation of iron ore to long distances with pipelines has brought a solution also for mining sector [2]. In addition to these materials, pipelines also transport hydrogen, and dangerous liquids such as LPG, gasoline and refined petroleum products [1], [6].

When considering the sectors where the pipes are used, the pipes could work at high pressures and have necessarily large diameters in order to decrease the cost and increase the efficiency of transport [2], [4]. Pipelines used in natural gas and oil transportation may be exposed to the plastic deformation caused by external forces such as landslides [7]. Another external factor is the fluctuation in pressure due to corrosive environment. In this case fatigue behavior gains importance in design [8]. The damages occurred in pipelines can cause many serious consequences from air, lake and river pollution to human injuries [1]. For these reasons, the pipeline material and the connected systems require good mechanical properties with having excellent welding and corrosion resistance that can withstand external impacts and negative effects [7], [8].

The main material of the pipes used in oil or natural gas transport is 97 % the hot rolled coils. Most of the line pipes used today are manufactured according to API 5L or EN ISO 3183 (DIN EN 10208-2) standards [1]. When the construction works of natural gas and oil pipelines in our country are examined; it is seen that API 5L X52 and API 5L X65 materials are commonly used (For example, in the Eastern Black Sea Natural Gas Pipeline project, API 5L X52 material was used and in Baku Tbilisi Ceyhan Crude Oil Pipeline API 5L X65 material was used.) [7]. For a very long time, API 5L X42, X52, X60, X65 steels have been used for these pipes, but for later high strength requirements X70 and X80 steels are developed and now preferred worldwide and also in our country. Trans-Anatolian Natural Gas Pipeline Project (TANAP), which has been realized in our country in recent years, is one of the important projects in which X70 steel is used [1], [7]. X70 pipeline steel is good in strength and toughness in addition to having great weldability and corrosion resistance [9]. X70 grade have been also widely used in the offshore pipeline industry for many years due to having great toughness and weldability properties. However, in terms of design and requirements, pipelines generally differ from offshore structures [10].

The durability of pipelines subjected to high pressure depends not only on the wall thickness of the pipe and the material structure but also on the quality of weld joints without cracks [11], [12]. Helical or longitudinal welded pipes produced by submerged arc welding (SAW) are mostly preferred in gas and oil transmission lines [7], [13]. Helical welded pipes are produced from hot rolled coils while longitudinal welded pipes are produced from plate or coil [1]. SAW; is used because of the easy control of the variables in the process, high quality, smooth welding, protection of the welding arc zone from the atmosphere and ease of automation process in welding process. The welding parameters used in submerged arc welding play an important role in the quality of the weld joint [11].

There have been many studies conducted on the mechanical properties of welded pipelines. However, studies on fatigue behavior have been one sided, focusing either on crack initiation or propagation. Searching fatigue properties in pipeline steels is a

serious concern as it is a long time operation and sudden failures could occur under cycling loadings created by pressure fluctuations in a corrosive environment during transportation [2], [8], [14]. This study has been conducted in order to have an integrated approach on fatigue behavior of welded pipelines. Within this scope, welded API 5L-X70M-PSL2 pipeline steel was subjected to the investigation.

For mechanical characterization tension tests, hardness measurements and charpy impact tests were carried out. Samples were examined with optical microscope and scanning electron microscope (SEM) microstructurally. Rotating bending fatigue tests of base material, weld and heat affected zone (HAZ) were performed according to the international ISO 1143:2010 Standard and S-N curves were plotted. Fracture surfaces were examined with SEM. Since pipeline steels eventually fracture due to crack propagation through the wall thickness of the pipe, it is important to study crack growth rate in fatigue failure [15]. In this context, striation spacings were measured with fractographic analysis and crack growth rates ( $da/dN$ ) were estimated for base metal, weld and HAZ. Stress intensity factor ( $\Delta K$ ) ranges were also calculated with striation counting method and  $da/dN$  vs.  $\Delta K$  curves were plotted in log scale for all test groups.



## **CHAPTER 2**

### **THEORY**

#### **2.1 Fatigue Phenomenon**

Fatigue is a very common damaging mechanism resulting in a catastrophic failure that occurs in materials and their structural components under dynamic and cyclic stresses for a long time. Due to the nature of that cycling stress in fatigue, crack initiation and propagation can occur at stress levels lower than the yield strength or tensile strength of the materials depending on the frequency, stress level and the stress pattern. Stress pattern can be axial, flexural or torsional. Owing to the safety issues in engineering applications, determination of fatigue properties of materials is a serious concern and many studies have been done on this subject [8], [14], [16], [17].

Fatigue process has three main stages, which are crack initiation, crack propagation and fracture, respectively. At crack initiation stage, small crack occurs due to stress concentration at crack nucleation sites at a very early stage of fatigue life. These sites contain pores, surface scratches, inclusions etc. Crack initiation can also be divided into three stages, which are cyclic slip, crack nucleation and micro crack growth. At crack propagation stage; the small crack enlarges incrementally due to the ongoing stress cycle and it is also called macro crack growth. At final stage; with the growing crack becomes critical dimension, very fast fracture eventuates [14], [16], [17].

Three different stress cycle graphs can be created to represent the variation of stress with time in fatigue by applying repetitive or fluctuated axial, flexural or torsional stresses [14], [16]. These stress cycles are reversed, repeated and random stress cycles. In reversed stress cycle, there is a fluctuation between maximum tensile stress

( $\sigma_{max}$ ) and minimum compressive stress ( $\sigma_{min}$ ) having the same value. Since tensile stress is considered positive while compressive stress is considered negative, the stress ratio (R) of reversed stress cycle is -1. The formula of stress ratio is given below [16], [17]:

$$R = \frac{\sigma_{min}}{\sigma_{max}} \quad \text{Eqn 1}$$

## 2.2 S-N Curves

Rotating bending fatigue test method is a widely used test method in order to reveal the fatigue properties of materials. With this method, the specimen is subjected to tensile and compression stresses due to simultaneous bending and rotation [16]. The tests are repeated at different stress levels for identical specimens. As a result, the number of cycles for failure corresponding stress level is obtained. With plotting these data, S-N curve that is a plot of stress amplitude (S) against number of cycles (N) is achieved. Stress amplitude and number of cycles are usually plotted on logarithmic scales or on logarithmic scale only the number of cycles is shown [14], [16], [17].

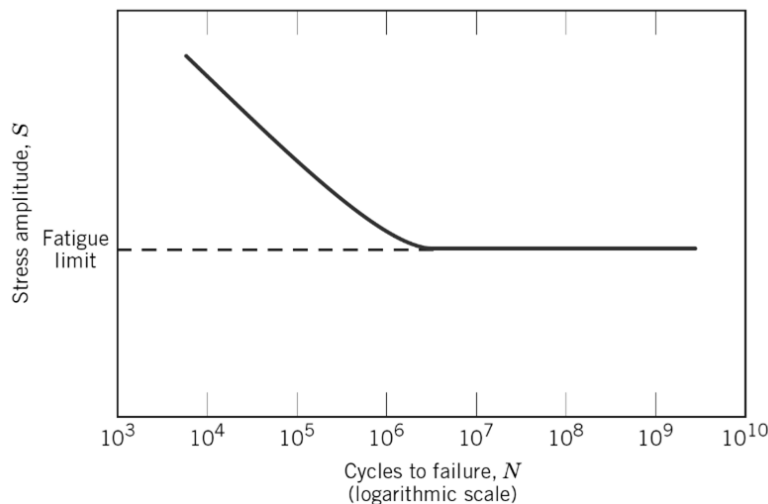


Figure 2.1. S-N curve for materials having fatigue limit

A typical S-N Curve for ferrous and titanium alloys is shown in Fig. 2.1. Unlike nonferrous alloys, for ferrous and titanium alloys there is a stress limit where S-N curve becomes horizontal. This straight part of the curve is known as fatigue or endurance limit. At any stress below this limit, fatigue failure does not occur [16], [17]. The fatigue limit for most steels changes generally from 2 to 10 million cycles. It is difficult to establish a very good overall relationship between fatigue properties and other mechanical properties of a material. Generally, a relationship is established between the fatigue limit under reversed stress cycle and the tensile strength. The ratio of fatigue limit to tensile strength is about 0.35 to 0.60 for most of the ferrous metals while it is approximately 0.20 to 0.50 for non-ferrous metals [16], [17].

### 2.2.1 Basquin's Equation

It is a power law equation and represents the linear relationship between the applied stress (S) and the number of cycles (N) on a log-log scale for the region of S-N curve where N changes from  $10^3$  to  $10^6$  cycles (for ferrous metals). The equation is given below [18], [19].

$$N_1 = N_2 \left( \frac{S_1}{S_2} \right)^{\frac{1}{b}} \quad \text{Eqn 2}$$

b is the slope of the log S-log N curve shown in Fig. 2.2.

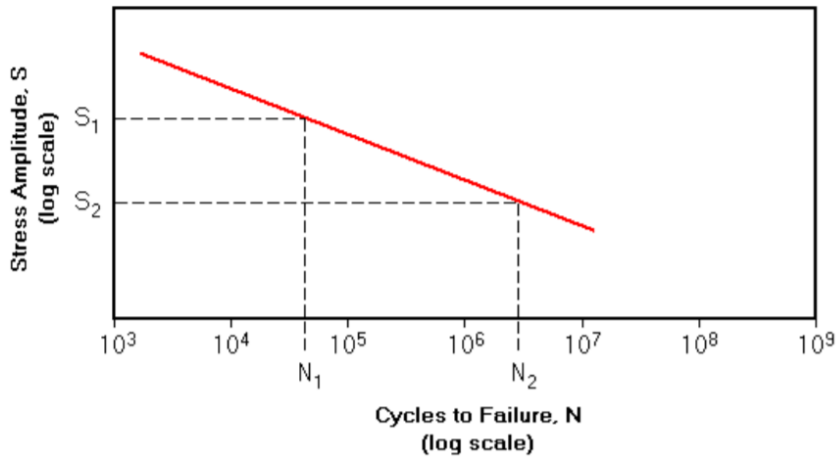


Figure 2.2. S-N curve on a log-log scale [19]

The slope is also called as Basquin slope and it is determined by using the following formula:

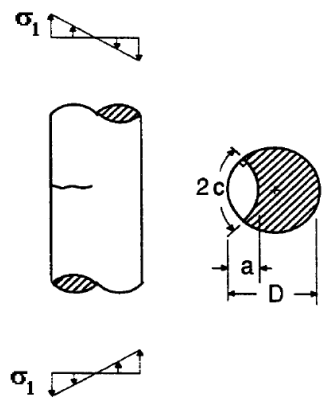
$$b = \frac{-(\log S_1 - \log S_2)}{(\log N_2 - \log N_1)} \quad \text{Eqn 3}$$

If Basquin slope and any pair of stress amplitude and number of cycles are given, the number of cycles to failure for a known stress amplitude could be calculated by using the slope equation [18], [19].

### 2.3 Crack Growth Rate

As it is mentioned in Section 2.1, fatigue failure occurs in three main steps and the second step is crack propagation. Since pipeline steels eventually fracture due to crack propagation through the wall thickness of the pipe, it is important to study crack growth rate in fatigue failure [15]. One of the approaches to determine the crack growth rate is using striation spacing by a fractographic analysis [20]. With this method, fracture surfaces are examined with SEM and stress intensity factor for a surface crack in a solid cylinder is calculated by below formulas given in Table 2.1 [21].

Table 2.1. Stress intensity factor solution for solid cylinder [21]

Stress Intensity Factor	$K_I = F_1 \sigma_1 \sqrt{\pi a}$
	$F_1 = G [0.923 + 0.199 Y^4]$ $G = 0.92 \left( \frac{2}{\pi} \right) \sec \beta \left[ \frac{(\tan \beta)}{\beta} \right]^{\frac{1}{2}}$ $Y = 1 - \sin \beta$ $\beta = \left( \frac{\pi}{2} \right) \left( \frac{a}{D} \right)$

## 2.4 Pipeline Steels

Today, high strength low alloy (HSLA) steels have been used in a wide range. In recent years, with the increasing use of natural gas, natural gas transportation has become very important and as a result, welded pipes made from high strength low alloy (HSLA) steel production has increased in both Turkey and all over the world [11].

As mentioned before, in this study API 5L-X70M-PSL2 pipeline steel which is a kind of HSLA was used for investigation. In American Petroleum Institute (API) Standard ‘API Specification 5L, 46th Edition, Line Pipe’, the abbreviations used to identify the steel are as follows:

- API 5L: It refers to the standard ‘API Specification 5L, 46th Edition, Line Pipe’. This specification is used to specify the properties of the pipe proper for the transport of oil, gas and water [22].
- X70: It refers to the steel grade and the chemical composition of the steel given in Table 2.2 [22].

Table 2.2. Chemical composition of steel grade X70M (PSL2 pipe with  $t \leq 25.0$  mm) [22]

Steel Grade	Wt % (max)								
	C <sup>b</sup>	Si	Mn <sup>b</sup>	P	S	V	Nb	Ti	Other
X70M	0.12 <sup>f</sup>	0.45 <sup>f</sup>	1.70 <sup>f</sup>	0.025	0.015	g	g	g	h,l

- M: It refers to the delivery condition of PSL2 pipe. The delivery condition could be thermomechanical rolled or thermomechanical formed [22].
- Thermo-mechanical control process (TMCP), which has been used since 1980's is a combination of thermo-mechanical rolling and accelerated cooling. This technique is developed for the improvement of strength, toughness and weldability of pipeline steels. The enhancement in mechanical properties are achieved with grain refinement in TMCP. The dominant microstructure attained with TMCP is uniform and fine acicular ferrite which plays a major role in increasing strength and toughness together. With this improvement in toughness, the risk of crack propagation decreases [23]–[25]. The comparison of microstructures of conventional rolled steel and TMCP steel is shown in Fig. 2.3 [26].

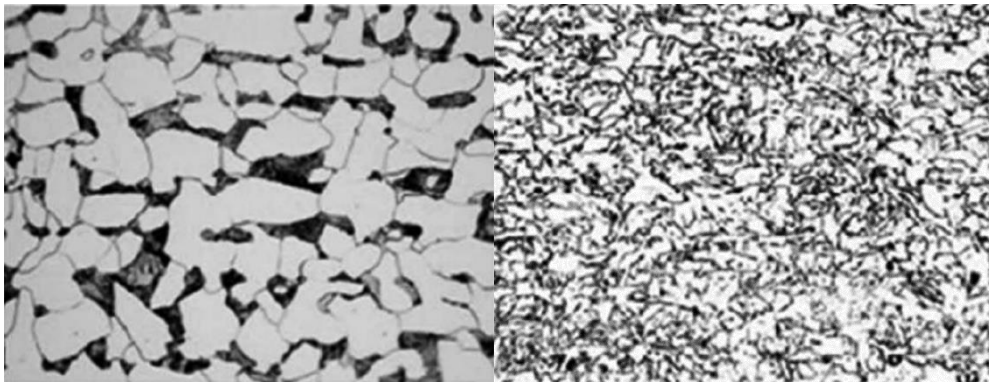


Figure 2.3. The microstructures of (a) conventional rolled steel and (b) TMCP steel [26]

- PSL2: It refers to the product specification level [22]
  - The suffix 'P' signifies a specified phosphorus range.

According to the API Specification, tensile requirements for Grade X70 PSL 2 are as follows [22];

- Yield Strength = 485 MPa (min) – 635 MPa (max)
- Ultimate Tensile Strength = 570 MPa (min) – 760 MPa (max)

## **2.5 Welding Process**

Welding processes for API 5L steels are defined in API standard ‘‘API Specification 5L, 46th Edition, Line Pipe’. The methods are grouped into two main headings; without filler metal and with filler metal. Welding processes without filler metal are; continuous welding, laser welding and electric welding while welding processes with filler metal consist of two methods; submerged-arc welding (SAW) and gas metal-arc welding (GMAW) [22]. The helical-welded X70 pipes used in this thesis study were produced with SAW method.

SAW is a high productivity welding process in which the weld metal is formed by the chemical and physical reaction of the base material, filler material (obtained from the electrodes and pressure is not used) and the welding powder (Fig. 2.4.) [13], [27], [28]. This coalescence of metals were produced by heating them with an arc zone. The arc zone and the molten metal are protected with a granular and fusible powder material against to the atmospheric contamination [13], [22], [28].

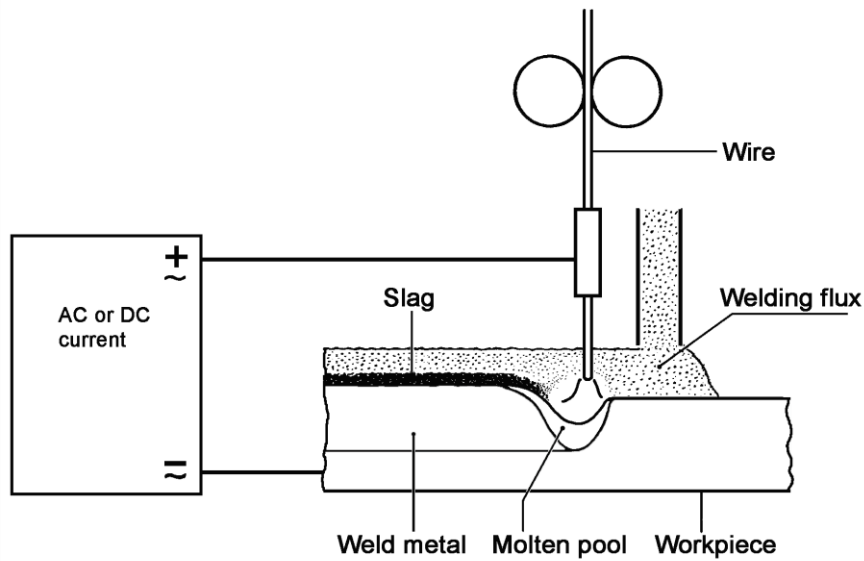


Figure 2.4. Schematic representation of submerged arc welding method [28]

Since SAW method is an automatic welding method (could be used also as a semi-automatic welding method [29]), the success of the process depends on substantially the welding parameters [7]. SAW is one of the most preferred welding method in line pipes due to the advantages mentioned below [7], [13], [27]–[29]:

- High performance in thick section materials
- Proper welding seam appearance and high welding quality
- High penetration depth; reducing the amount of filler material
- Labor, time and energy saving
- High welding speed due to high arc time factor
- High rate of metal deposition (due to high welding currents)
- Advanced working environment when compared with the other arc welding methods
- High melting efficiency

The tensile strength requirement for the Weld Seam of PSL 2 Pipe welded by SAW method is 570 MPa [22].

## **2.5.1 The Effects of Welding on Microstructure**

The weld metal and the heat affected zone (HAZ) together form the weld joint. HAZ is defined as the base material structurally affected by thermal cycle of welding process. The composition of the HAZ is the same as the base material, while the microstructure of the HAZ depends on base material and thermal cycle of the welding process. The properties of the HAZ region play an important role in the performance of the weld seam. The difference in strength between the weld metal, HAZ and the base material produces strain concentration in the region having lowest strength. The base material, the maximum temperature reached in the welding process and the corresponding cooling rate are the main factors that cause HAZ to be divided into several sub-regions. These sub-regions have different microstructures and this difference in microstructures leads to different mechanical properties [11], [29]. Toughness for high strength pipeline steels has always been the focus of research interest because it differs throughout the weld joint. Many studies underline the importance of HAZ having the lowest toughness in the weld joint. Coarse grains resulting from welding thermal cycle adversely affect the toughness in the HAZ region [11], [29]. Additionally, the microstructure of HAZ in welded steels are found to be sensitive to different types of cracking particularly cold cracking [29].

### **2.5.1.1 Coarse Grained Region**

The region closest to the fusion line is the grain coarsened region which is called as HAZ1 in some sections of this thesis. This region experiences a thermal cycle between 1100 – 1530 °C above the grain coarsening temperature of austenite. The importance of HAZ1 stems from the widespread appearance of cold cracking in this region. Depending on the increase in austenite grain sizes, some undesirable microstructures such as upper bainite, twinned martensite, martensite/austenite islands and widmanstatten ferrite may occur. These microstructures cause cold

cracking as a result of embrittlement of them. Also during cooling, due to the transformation of coarsened austenite grains into coarse structure, toughness and strength of the HAZ decrease [29].

The effect of peak temperature and composition on grain coarsening is found to be much more than the effect of time above the temperatures where grain coarsen [29].

### **2.5.1.2 Grain Refined Region**

In this region, which is called as HAZ2 in some sections of this thesis, grain size is very small compared to the coarse grained region since grains cannot coarsen between 900 – 1100 °C. Actually, grains recrystallize in the grain refined region. In cooling, due to the not complete dissolution of carbides and nitrites, fine-grained austenite and insoluble carbides and nitrides could produce a fine-grained ferrite and a second component. Depending on the composition and cooling rate of the steel, pearlite, bainite or martensite/austenite islands can occur as a microstructure of this second component. Contrary to HAZ1, the mechanical properties such as toughness and strength in HAZ2 are not influenced negatively relative to the parent material [29].

### **2.5.1.3 Inter-Critical Region**

Inter-critical region, which is also known as partially transformed region, is called as HAZ3 in some sections of this thesis. In this region, the reached temperature is between 750 – 900 °C temperature ranges. At these temperatures, pearlite can transform to austenite partially because of lower transformation temperatures. During cooling, due the transformation of these austenite regions, microstructures that may occur are pearlite, upper bainite, autotempered martensite or high carbon martensite according to the rate of cooling. Carbon content can affect the martensitic islands to embrittle [29].

#### **2.5.1.4 Base Metal**

In the base metal region, no microstructural changes can be observed which can be distinguished by optical microscopy since the temperature is below 650 °C.



## **CHAPTER 3**

### **LITERATURE REVIEW**

Fatigue failure in pipelines can be handled in two respects; one is crack initiation and the other is crack growth, which are the main stages of fatigue failure [14]. In this literature review, fatigue failure studies of pipelines used in transportation and commonly used testing methods will be reviewed based on crack initiation. In addition, special attention will be given on fatigue failure behavior of X70 pipeline steel, which was tested in this thesis study.

There are also studies investigating microstructural and mechanical behavior of X70 steel pipes manufactured with submerged arc welding. These studies will also be mentioned in order to understand the effect of welding on basic mechanical properties of base metal, weld zone and HAZ.

#### **3.1 Welding Based Studies**

In a study conducted by Tas Z. et.al [12], the mechanical properties of X70 pipeline steel were examined before and after submerged arc welding process. In addition, weld zone was investigated in detail. In order to understand if there is a surface or subsurface defect in the joints after welding process, visual inspection and nondestructive test methods were carried out. As a result of the examinations, no welding defects were observed. According to the tensile test results, the yield and the tensile strength of the weld material were higher than the base material. As a result of hardness measurements, hardness values from highest to lowest were observed in weld material, heat affected zone (HAZ), and base material, respectively. For the toughness measurements, notched bend impact test was carried out. The results of this test showed that toughness values were higher for base material, HAZ, and weld material, respectively unlike the hardness values.

In an another study done for the investigation of microstructural and mechanical properties of X70 steel produced by submerged arc welding, Aksöz S. et.al [7], examine the mechanical properties of X70 steel with hardness, tension, charpy impact and bending tests. According to the results of the hardness tests, the highest hardness values were found in the weld metal and the lowest hardness values were determined in the HAZ region. As a result of tension tests, yield and ultimate tensile strength values of welded specimens were found to be higher than the values of the base material. Charpy V-notch impact tests were carried out at  $-15\text{ }^{\circ}\text{C}$ . The specimens were prepared from weld material, fusion line, FL + 2 (2 mm from the fusion line and on the base material side), FL + 5mm (5 mm from the fusion line and on the base material side), and base material. In the impact energy measurements performed in the weld metal, FL, FL + 2, FL + 5, and the base material regions respectively, it is seen that the amount of energy increases from the welding metal to the base material. In addition, welded samples were subjected to bending tests and as a result, macro defects such as cracking, tearing etc. were not observed.

In a study conducted by Apay S. et.al [11], the weld region of API 5L X70 steel which was submerged arc welded with different welding parameters was examined. Tensile tests, Charpy impact (V notched) tests, hardness measurements, macrostructural examination and radiography for NDT were used for the examination of the welded regions. According to the tensile tests results, fracture occurred in base metal for all specimens having different welding parameters. The tensile strength of the specimens provide the tensile requirements of API 5L standard. The hardness measurements showed that hardness values increased from the base material towards the welding metal and the increase in heat input decreased the hardness of heat affected zone (HAZ). When the results of impact test were examined, toughness values of the specimen welded with higher heat input was higher than the toughness values of other specimens. It is observed that toughness of the HAZ and the weld metal inversely proportional to the hardness values measured from the same regions.

In this study conducted by Akay A.A. et.al [13], X60, X65 and X70 steel were welded by submerged arc welding method using two different weld powder and wire. For examination of the weld zone, visual inspection, ultrasonic testing, tensile and bending tests, hardness and macrostructural studies were performed. As a result of tensile tests it is observed that fracture occurs in base metal region in all specimens and the tensile properties of weld were found to be higher than the base metal as in previous studies mentioned above. In all specimens, the highest hardness values were measured in weld region while the lowest values were measured in base metal. According to the bending tests, defects such as cracks, tears etc. were not observed on weld zone. The study shows that weld powder and wire affects the mechanical properties of the weld joint. X70 steel welded with S2Mo wire and P223 powder had the best mechanical properties of all.

### **3.2 Fatigue Behavior Based Studies**

In the study done on the fatigue behavior of welded steel pipes by Simion P. et.al [14], in order to investigate and establish a relationship between the factors affecting the fatigue properties of longitudinal welded pipes, several test were performed such as; hardness measurement, tension and impact tests and microstructural analysis by optical microscopy and SEM. Some of the specimens were prepared from welded pipes subjected to heat treatment since heat treatment on weld seam is used to eliminate the residual stress and repair the structure. According to the tensile test results, elongation values of specimens with heat treatment are 30 % higher than the ones without heat treatment while the values of tensile strengths are a little bit lower. The considerable difference is that the impact energies of specimens with heat treatment are twice of the specimens without heat treatment.

From the hardness versus distance graphs shown in Fig. 3.1, it is seen that hardness values decrease noticeably with heat treatment and this results coincides with the noticeable drop in toughness in weld seam. Another considerable change with heat treatment is that; the microstructures of the base metal, heat affected zone and the

weld seam are quite homogeneous and consist of ferrite (polygonal) and pearlite [14].

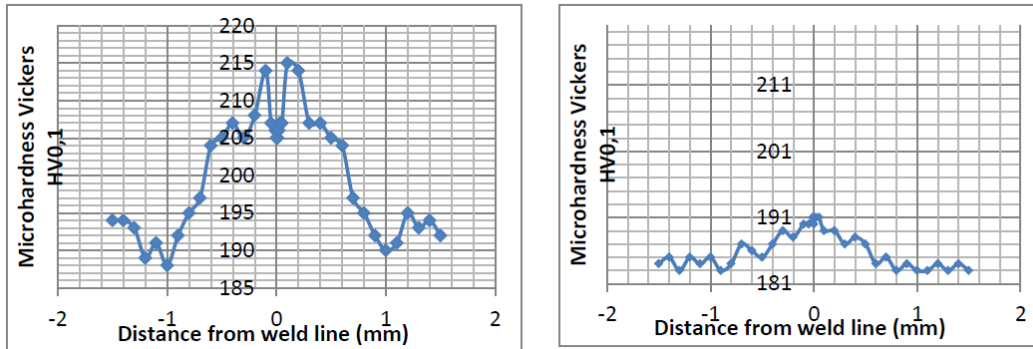


Figure 3.1. Hardness values of welded pipes; (a) without heat treatment, and (b) with heat treatment [14]

In Fig. 3.2, the S-N curves of the specimens taken from welded pipes with and without heat treatments are compared. It is observed that the specimen subjected to heat treatment has better fatigue life at the same stress levels compared to the specimens without heat treatment [14].

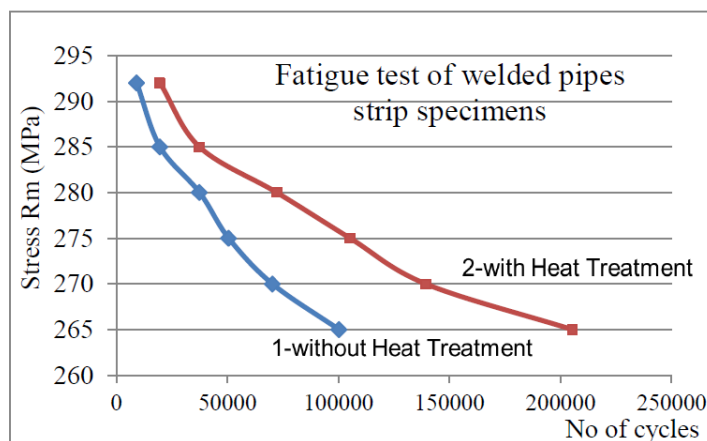


Figure 3.2. S-N curves for strip specimens taken from welded pipes with and without heat treatment [14]

The study shows that there are many factors that can affect the fatigue behavior of longitudinal welded steel pipes but the most important ones are surface quality, pipe geometry and the stress concentration because of welding. Another important conclusion of this study is that there is a noticeable relationship between toughness and fatigue resistance [14].

Mikova K. et.al [8], investigate the effect of severe shot peening (SSP) on the fatigue properties of X70 Steel in their research. For this purpose several test methods were used such as; roughness, hardness, measurement of residual stress with X-ray diffraction (XRD), rotating bending fatigue tests, and fractographic analysis by SEM. Residual stress induced by SSP was analyzed by XRD and the results show that depth of the material affected by this stress increases. According to the results of microhardness measurements in Fig. 3.3, the hardness of the surface has been found to be highest when material is severe shot peened and the hardness values decrease gradually from the surface to the depth along the material. Roughness measurements represents that SSP leads to increase in surface roughness.

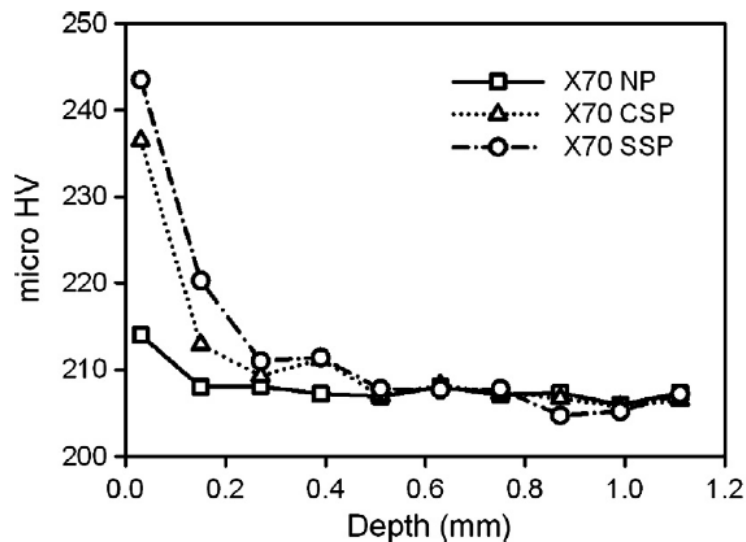


Figure 3.3. Microhardness values of different series of X70 steel specimens; subjected to SSP, Conventionally shot peening (CSP) and not peened [8]

For fatigue analysis, rotating bending fatigue tests were conducted for SSP, CSP and not peened specimens. Fatigue tests results for notched and smooth specimens are shown in Fig. 3.4 and 3.5. Both figures confirm the improvement in fatigue strength with severe shot peening. This improvement is considered to be the result of generating nanostructured surface layer and deeper residual stress produced [8].

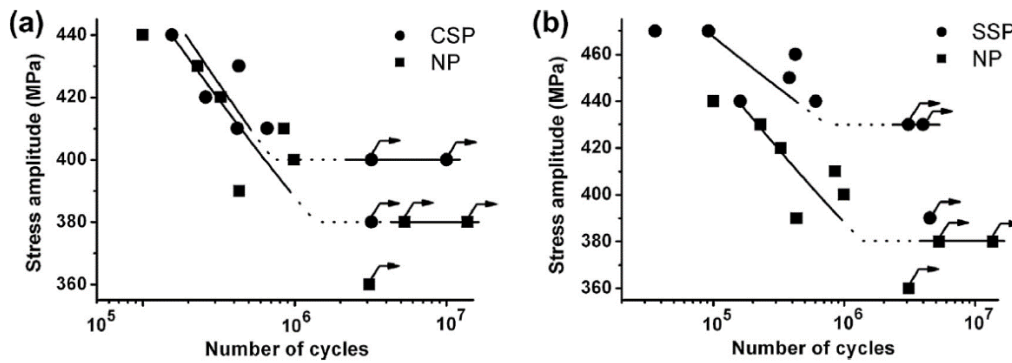


Figure 3.4. S-N curves for smooth specimens (a) CSP and not peened, and (b) SSP and not peened [8]

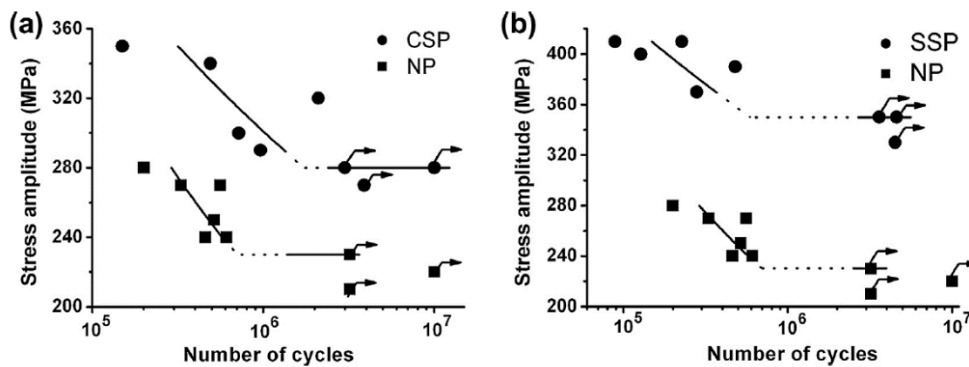


Figure 3.5. S-N curves for notched specimens (a) CSP and not peened, and (b) SSP and not peened [8]

In a study conducted by Gajdos L. et.al [5], fatigue properties of X70 in crude oil was subjected to investigation. The fatigue behavior in crude oil was compared with

fatigue behavior in separated water, air and alkaline solution. Fig. 3.6 shows the S-N curves of for X70 steel at different environments. The results of this study shows that crude oil doesn't affect the fatigue behavior of X70 steel noteworthy. However, separated water has a considerable negative effect on the fatigue properties of X70 steel as can be seen in Fig. 3.6.

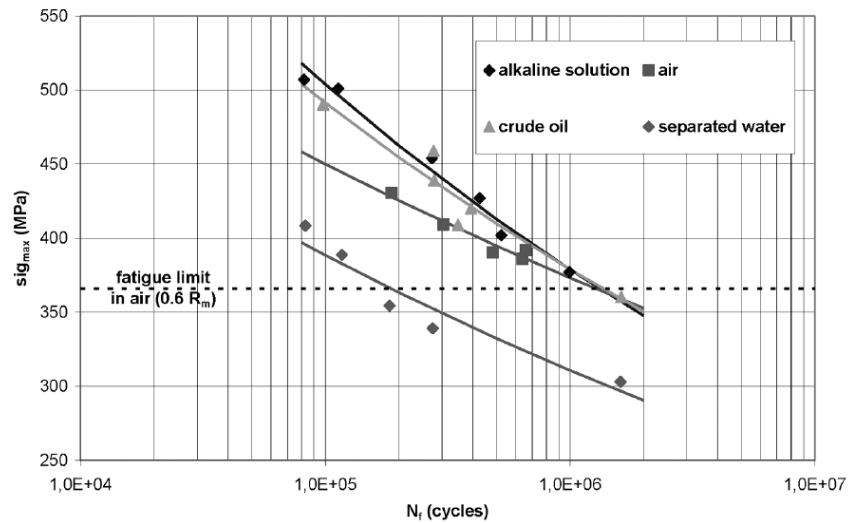


Figure 3.6. S-N curves for X70 steel at different environments [5]

It is also substantial to consider fatigue failure behavior for the transport of pressurized hydrogen gas along steel pipelines. In this manner, there are many hydrogen-based studies conducted for pipeline steels in order to see the effect of hydrogen on the fatigue properties of the pipeline steels [6], [15], [30], [31].

In a study conducted by Capelle, J. et al [6], the effect of hydrogen on mechanical properties of pipelines steels (X52, X70 and X100) was investigated performing fatigue and fracture toughness tests. Three-point bending test machine providing hydrogen charging was used for fatigue test. Crack initiation data were detected by acoustic emission. Fig. 3.7 presents S-N curves for X52 steel at air and hydrogen environment and hydrogen affects the fatigue life negatively with decreasing the number of cycles at the same stress levels. The results of this study shows that fatigue life could be diminish by 70 % for the X52 steel because of hydrogen influence.

Another important effect of hydrogen is the impact on crack initiation time. Crack growth is also promoted by hydrogen.

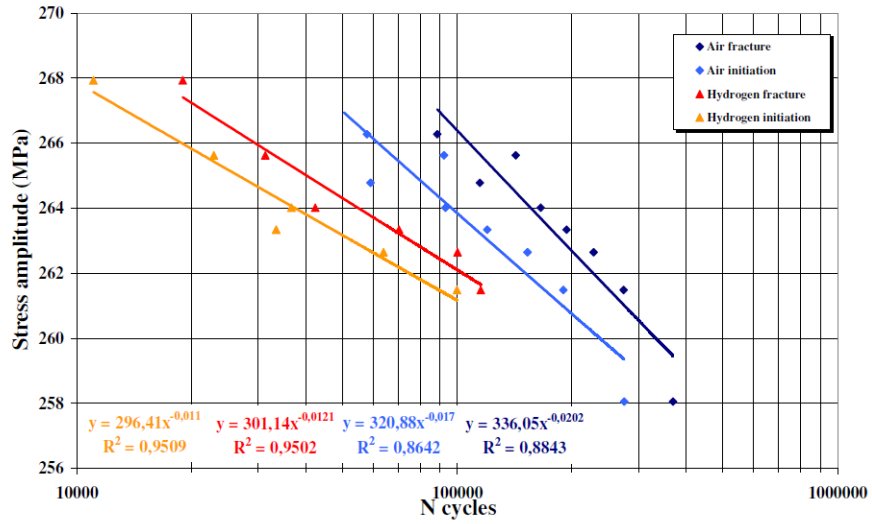


Figure 3.7. S-N plot of API X52 steel at air and hydrogen environment [6]

## CHAPTER 4

### EXPERIMENTAL PROCEDURE

#### 4.1 Material and Production Process

As mentioned before, in this study API 5L-X70M-PSL2 pipeline steel, which is a kind of HSLA, was used for investigation. According to the Mill Test Certificate of X70 steel issued according to EN10204 3.1, it was produced by basic oxygen process, vacuum degassing and calcium treated process, and ferrite grain size is 13.0. The average grain diameter is 3.97  $\mu\text{m}$  corresponding to the ASTM grain size number 13 [32]. Chemical composition of the API 5L X70 steel is shown in Table 4.1. When the chemical composition results in Table 4.1 were compared with the API chemical composition specifications given in Section 2.4 (Table 2.2), the steel meets the requirements of the API Specifications 5L.

Table 4.1. Chemical composition of API 5L X80 steel

	C	Si	Cu	Fe	Mn	Mo	P	S	Ni	Cr	V	Nb	Al
Wt %	0.06	0.39	0.04	97.43	1.58	0.11	0.01	<0.01	0.05	0.21	<0.01	0.06	0.03

#### 4.2 Welding Process

In this thesis, welded and non-welded sections taken from the pipes of a company producing pipes with SAW method were examined. The reason for preferring welding in factory conditions rather than welding in laboratory environment is the different cooling rates in laboratory and factory conditions. A single pipe, which is produced in the factory, is about 14 meters. The cooling rate of a 14-meter steel is very difficult to obtain with laboratory pieces. Very large pieces should be used and

that is not possible in laboratory. Also due to high cooling rates in factory conditions, there is a possibility of austenite and martensite formation, which cause a drop in toughness. Another issue to consider is the different loads occur during helical welding in the factory. It is also not possible to obtain these loads in laboratory conditions.

The company produced helical-welded pipes from hot rolled X70 coils (Fig. 4.1) with SAW method (Fig. 4.2).



Figure 4.1. Hot rolled coil of X70 Steel



Figure 4.2. Submerged arc welding process; (a) welding, (b) cooling, (c) welded pipe

S2 Mo welding wire was used as an electrode and P223 welding powder was used as a protective powder during the joining processes. Welding parameters, welding geometry and the chemical composition of the weld material are given in Table 4.2, Fig. 4.3 and Table 4.3, respectively.

Table 4.2. Welding parameters

	Current (A)		Voltage (V)		Welding speed (cm/min)
	DC	AC	DC	AC	
Inside	$1000 \pm 100$	$675 \pm 67.5$	$29 \pm 2$	$32 \pm 2$	$130 \pm 13$
Outside	$1100 \pm 110$	$650 \pm 65$	$30 \pm 2$	$34 \pm 2$	$130 \pm 13$

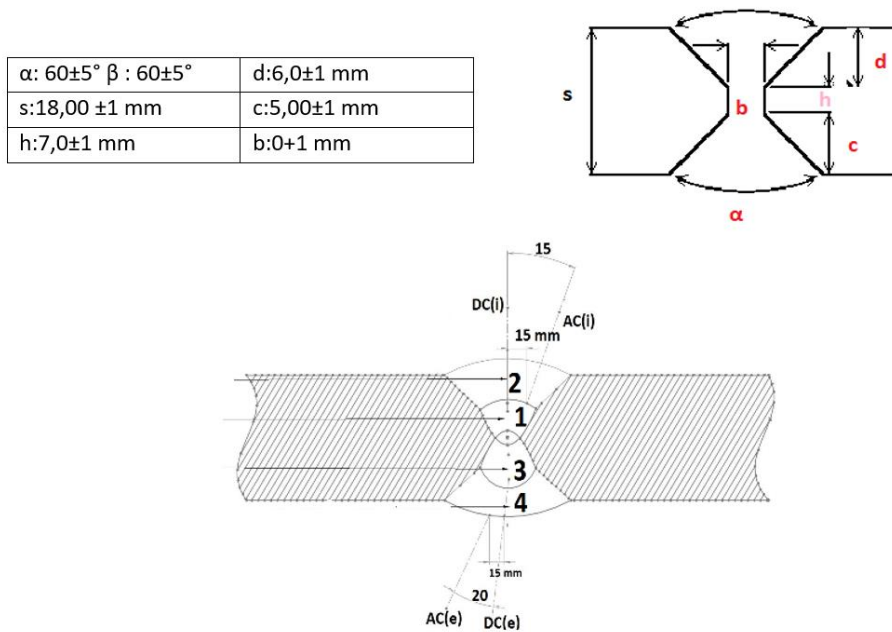


Figure 4.3. Welding groove geometry

Table 4.3. Chemical composition of weld metal

	C	Si	Cu	Fe	Mn	Mo	P	S	Ni	Cr	V	Nb	Al
Wt %	0.06	0.39	0.07	97.43	1.48	0.24	0.01	<0.01	0.05	0.17	<0.01	0.04	0.02

### 4.3 Specimen Directions Used in Experimental Procedure

Fig. 4.4 shows weld and rolling directions while Table 4.4 shows the specimens' directions for each of the experiments conducted.

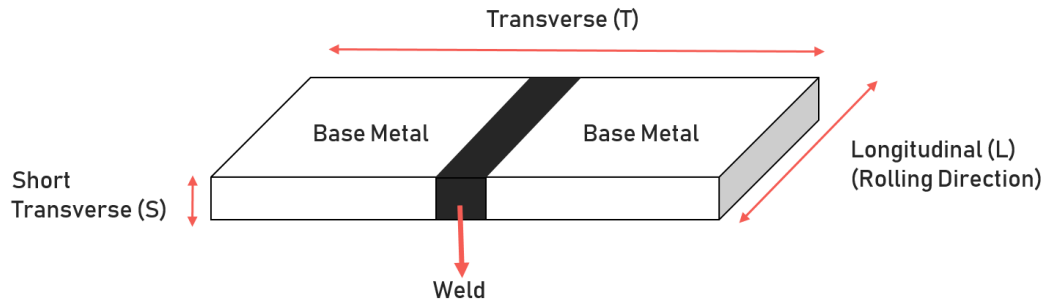


Figure 4.4. Directions of weld and rolling

Table 4.4. Specimen directions for the experiments

<b>Experiments</b>		<b>Directions</b>
Microstructural Analysis		Transverse and Longitudinal
Tensile Test	Base Metal	Transverse
	Welded Metal	Transverse and Longitudinal
Hardness Measurement		Transverse
Charpy Impact Test		Transverse
Rotating Bending Fatigue Test		Transverse
Strain Gage Measurement		Transverse

#### 4.4 Microstructural Analysis

Two different specimens were prepared in transverse and longitudinal directions for microstructural analysis with optical microscope. Specimens were etched with 2 % Nital. The specimen prepared in transverse direction comprises regions of weld and HAZ (Fig. 4.5). HAZ has three different microstructure due to different cooling rates during welding. So all these regions which were called as HAZ1 (coarse grained region), HAZ2 (grain refined region) and HAZ3 (inter-critical region) were subjected to investigation. The specimen prepared in transverse direction was also examined with SEM.

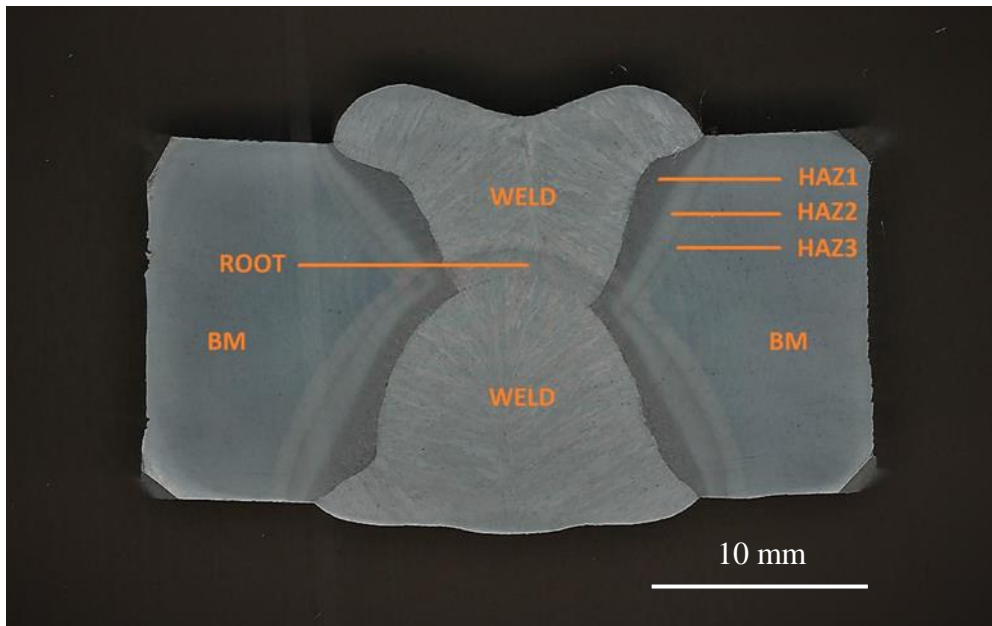


Figure 4.5. The specimen prepared for microstructure analysis in transverse direction

## 4.5 Mechanical Analysis

### 4.5.1 Tension Test

The mechanical behavior of HSLA X70 steel was firstly investigated in regards of tensile properties. Tensile properties of both base metal and weld zone were examined with 100 kN Instron Universal Tension/Compression Testing Machine (the load cell of the machine is certified) according to ISO 6892-1:2016 Standard.

#### 4.5.1.1 Base Metal

Two tensile test specimens were prepared from the base metal region of X70 Steel Pipes (Fig. 4.6). The specimens were prepared in transversal direction that is perpendicular to the direction of rolling.

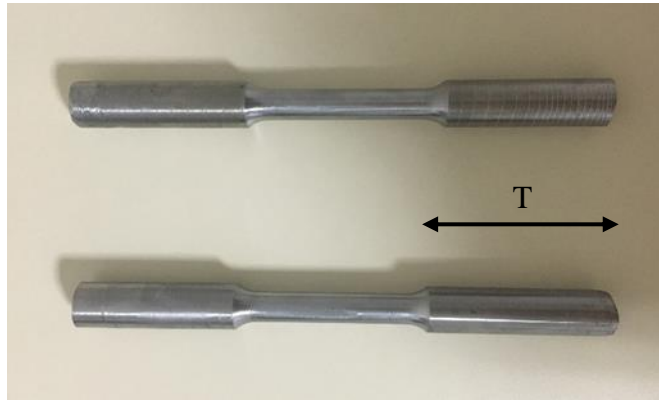


Figure 4.6. Tensile test specimens prepared from base metal region of X70 steel

#### 4.5.1.2 Weld Zone

Two tensile test specimens were prepared from the weld zone of X70 Steel Pipes. One was prepared in longitudinal direction (specimen 1) while the other one was in transverse direction (specimen 2) as can be seen in Fig. 4.7. In order to see the weld region in the test specimen prepared in transverse direction, the specimen was etched with 10 % Nital. The weld section of the specimen prepared in transverse direction is seen in Fig. 4.8.

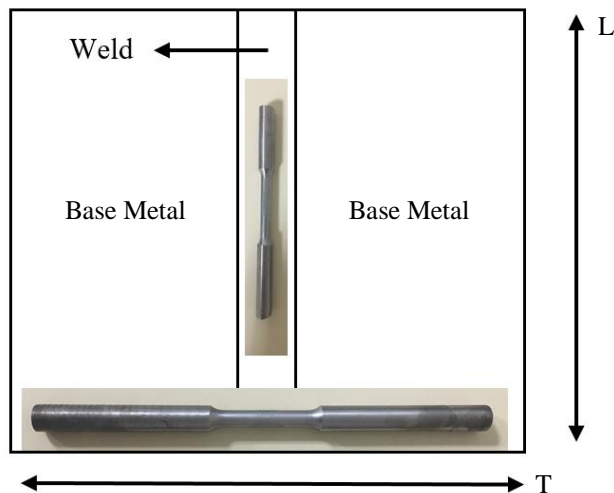


Figure 4.7. The directions of the tensile test specimens prepared from weld region of X70 steel

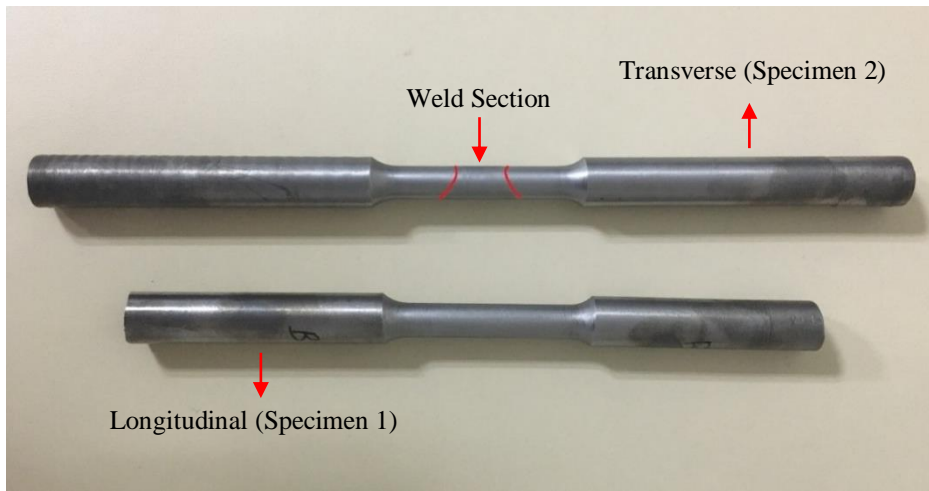


Figure 4.8. Tensile test specimens prepared from weld zone of X70 Steel

#### 4.5.2 Hardness Measurement

Vickers hardness test method was used to measure the hardness values of base metal, heat affected zone and weld metal according to ISO 6507-1:2018 Standard. The specimen prepared in transverse direction for microstructural analysis was also used for hardness measurements. In order to achieve accurate results, hardness values were taken from three different lines as shown in Fig. 4.9.

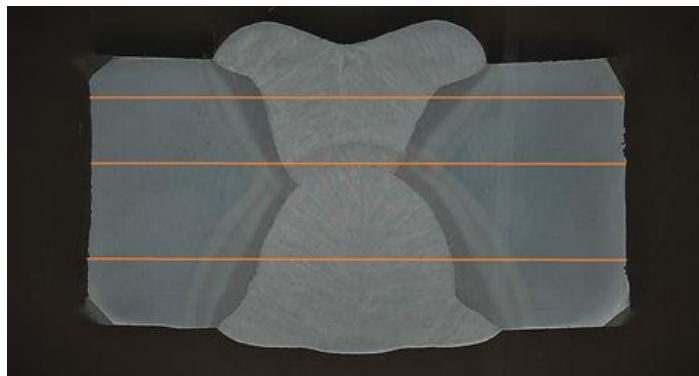


Figure 4.9. Lines where the hardness data were taken along; (a) upper line, (b) midline, (c) lower line

### 4.5.3 Charpy Impact Test

Charpy impact specimens with a V-notch were prepared from base metal, HAZ and weld metal according to ISO 148-1:2016 Standard in transversal direction. For the analysis of HAZ, one type of specimens were prepared from 1 mm right of the fusion line and the other type of specimens were prepared 2 mm right of the fusion line. They were mentioned as fusion line 1 (FL1) and fusion line 2 (FL2) as shown in Fig. 4.10.

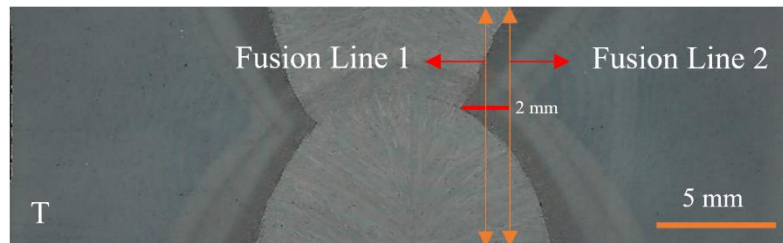


Figure 4.10. Notch locations; fusion line 1 and fusion line 2

In each type of specimens, three samples were prepared with a size of 10 mm x 10 mm x 55 mm and a V notch of 2 mm deep. In a study conducted by Aksöz et.al. [7], it is indicated that test temperature can be changed under the influence of environmental conditions as specified in ASTM A370 [7]. In our country, the lowest temperature to be exposed to the pipeline under service conditions can be about -15 °C at the transition points of the pipelines, considering that the continental climate is dominant. -30 °C and room temperature were chosen as test temperatures in order to stay in the continental climate temperature ranges. Charpy V-notch impact tests were carried out using certified Tinius Olsen Pendulum Impact Tester (406 J).

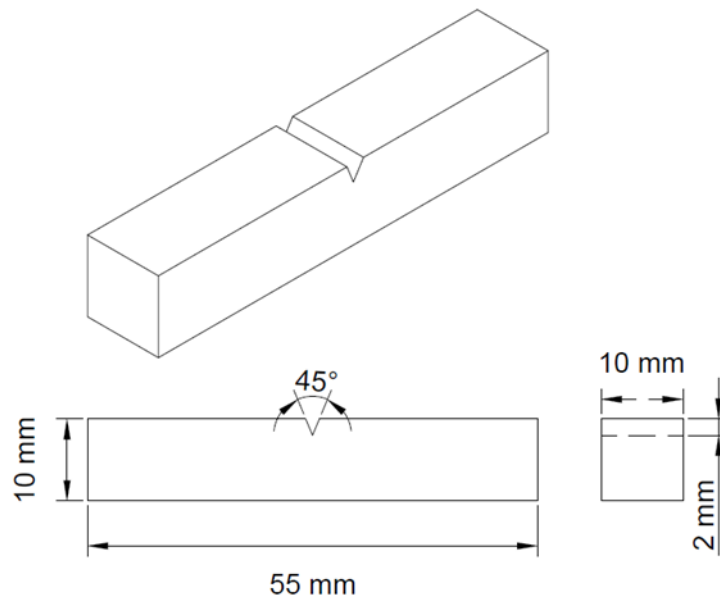


Figure 4.11. Charpy V-notch specimen geometry and dimensions

#### 4.6 Rotating Bending Fatigue Test

Rotating bending fatigue tests were conducted according to the ISO 1143:2010 Standard at room temperature and a nominal frequency of 30 Hz. The rotating bending testing machine with a servomotor having capacity of maximum 3000 rev/min was used for the tests (Fig. 4.12).



Figure 4.12. Rotating beam fatigue test machine

Identical specimens in hourglass type were prepared in transversal direction with base metal, HAZ and weld metal are in the middle of the specimen. All were subjected to single point loading with a stress ratio (R): -1. This value of stress ratio indicates that maximum tensile stress and minimum compressive stress having the same value with negative signs as it is mentioned in Section 2.1. This is achieved by subjecting the specimen to simultaneous rotation and bending. The resulting sinusoidal curve of stress vs. time graph for stress ratio (R): -1 is shown in Fig. 4.13. Stress amplitude corresponding to load is equal to the magnitude of tensile or compressive stress according to the formula shown below [16].

$$\sigma_a = \frac{\sigma_r}{2} = \frac{(\sigma_{max} - \sigma_{min})}{2} \quad Eqn 4$$

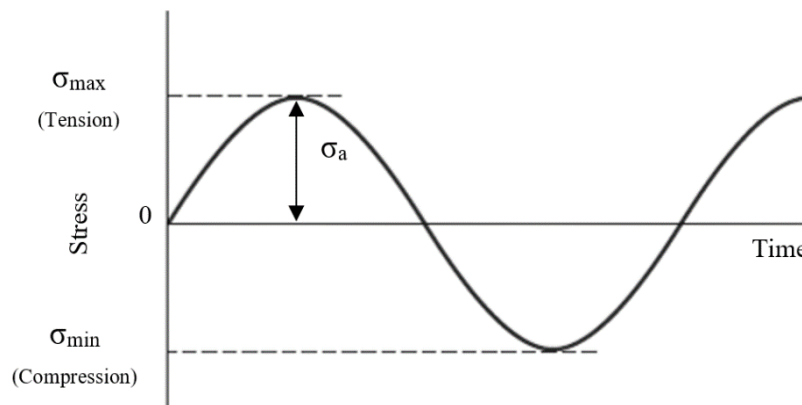


Figure 4.13. Stress vs. time graph for stress ratio (R): -1

The geometry of hourglass type specimen, the moment (M) diagram and the stress ( $\sigma$ ) distribution along the specimen is shown in Fig. 4.14. Stress reaches maximum value at the center of the specimen where the cross section is smallest while moment increases along the specimen. The maximum stress reached at the smallest cross section is obtained at the surfaces. The distribution of stress at the cross section is shown in Fig. 4.15.

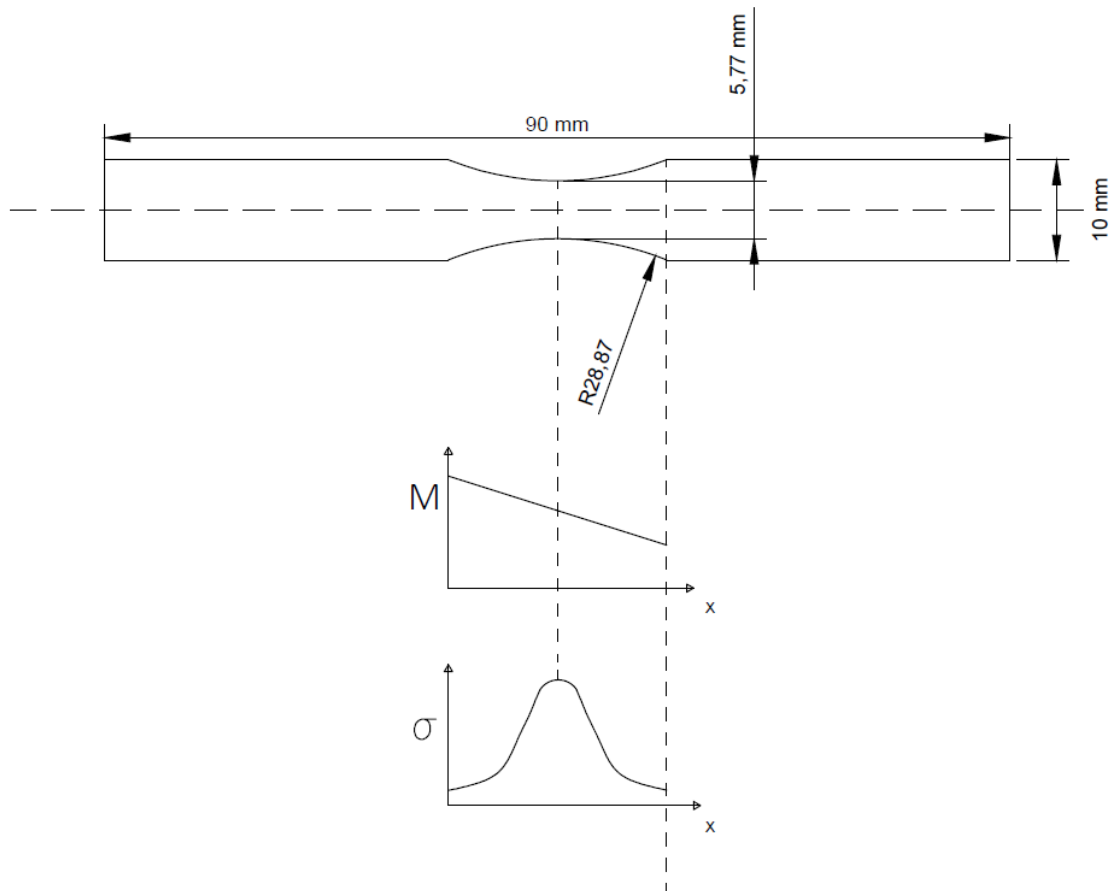


Figure 4.14. Geometry of hourglass type specimen and the corresponding moment ( $M$ ) and stress ( $\sigma$ ) diagrams as a function of the distance ( $x$ )

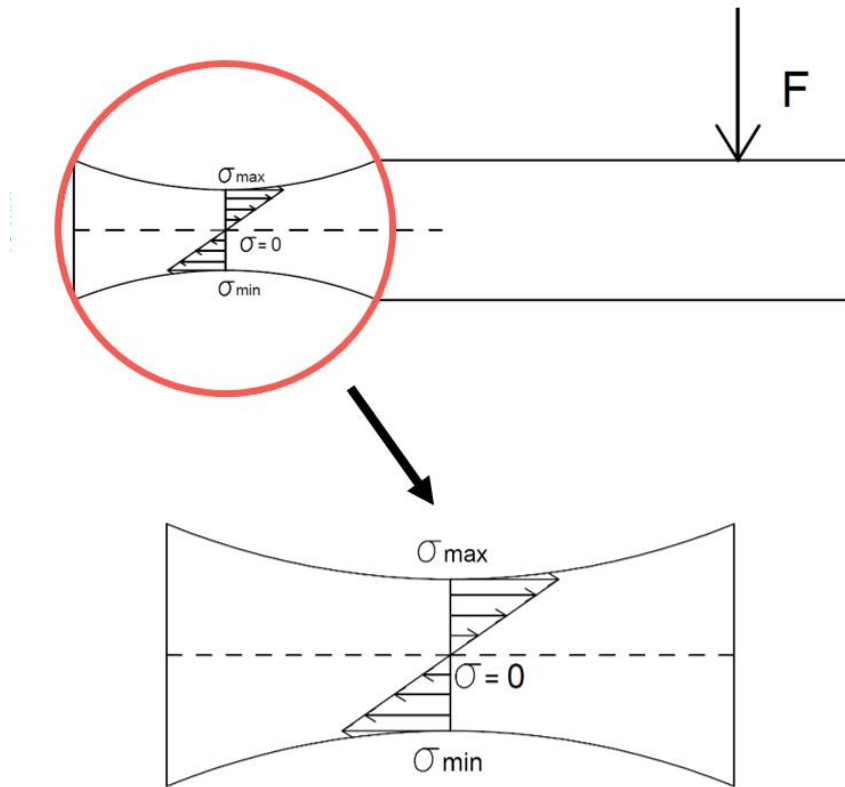


Figure 4.15. Stress distribution along the smallest cross section of the specimen

In the welded specimen, to see if the weld is coincided with the center of the specimen, it was etched with 10 % Nital. As can be seen from Fig. 4.16, the welded section is at the center of the specimen.

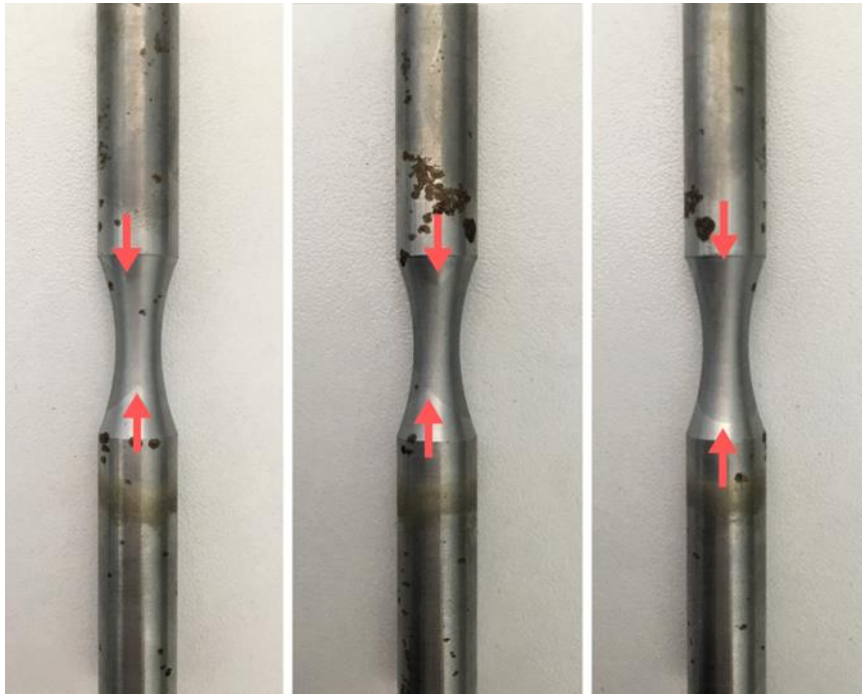


Figure 4.16. Specimens with welded section

#### 4.7 Strain Gage Measurement

In order to confirm the calculated stress corresponding to a given load on a rotating beam test machine, strain gage method was used. As shown in Fig. 4.17, strain gage was located on the top surface of a specimen with a specific geometry (Fig. 4.18) prepared for the strain gage measurement. For a reliable measurement, the mid-section of the specimen was prepared in rectangular geometry unlike the rotating bending specimen shown in Fig. 4.14. The reason of this specific geometry is that it is not possible to locate the strain gage at the center of the hourglass type specimen with such diameter.

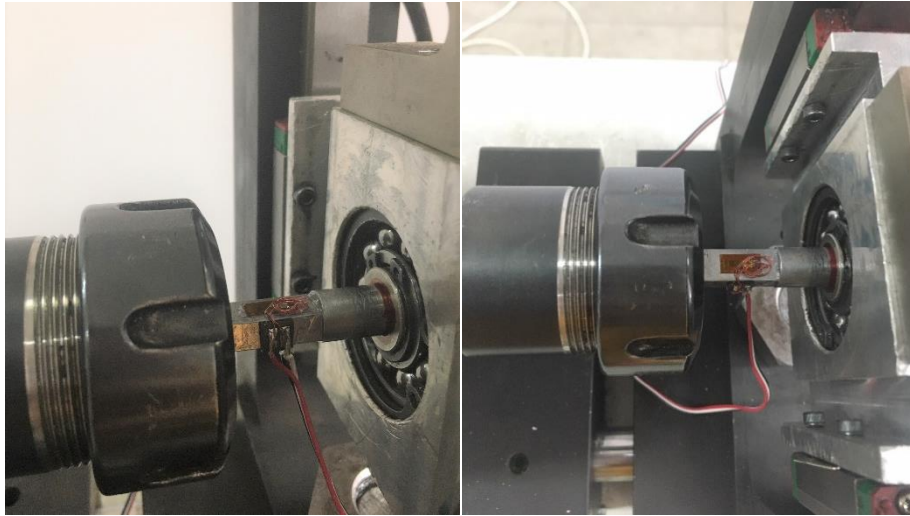


Figure 4.17. The specimen with strain gage on rotating beam fatigue test machine

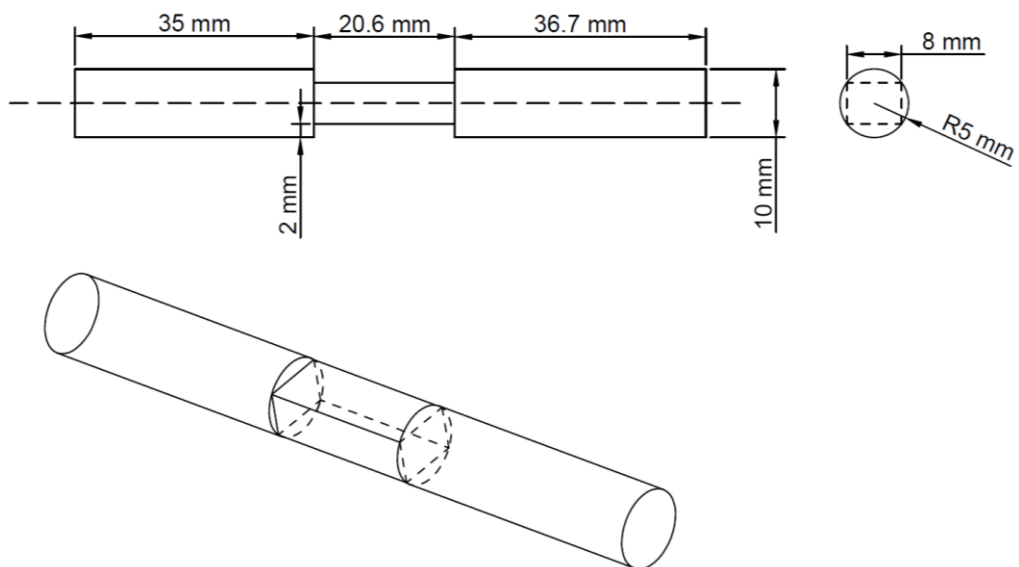


Figure 4.18. Geometry of specimen prepared for strain gage analysis

For the experiment, specimen was loaded with different loads and the strain values corresponding to these loads were measured as shown in Fig. 4.19. The graph in Fig. 4.20 shows the strain measurements vs. time graph for the load of 222 N. The Fig. 4.21 shows the minimum and the maximum strain measured for the same load.

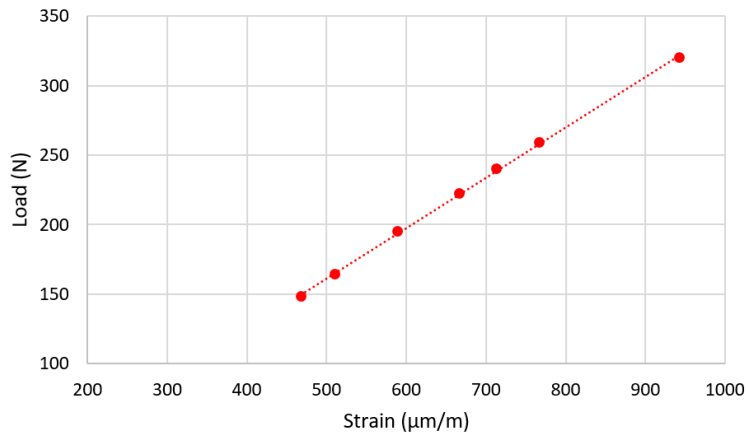


Figure 4.19. Load vs. strain graph of strain gage measurements

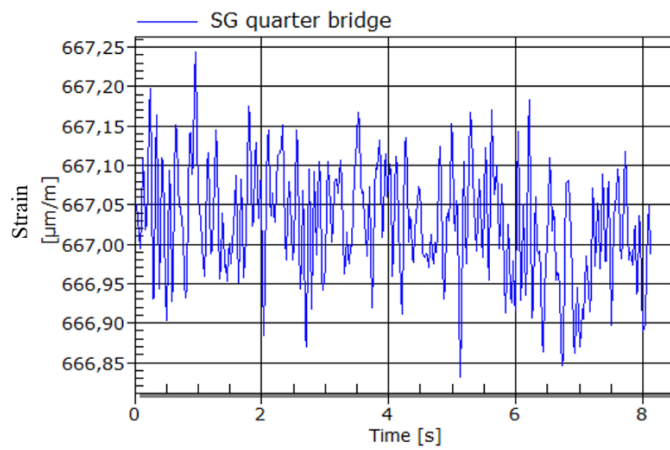


Figure 4.20. Strain vs. time graph for the specimen loaded with 222 N

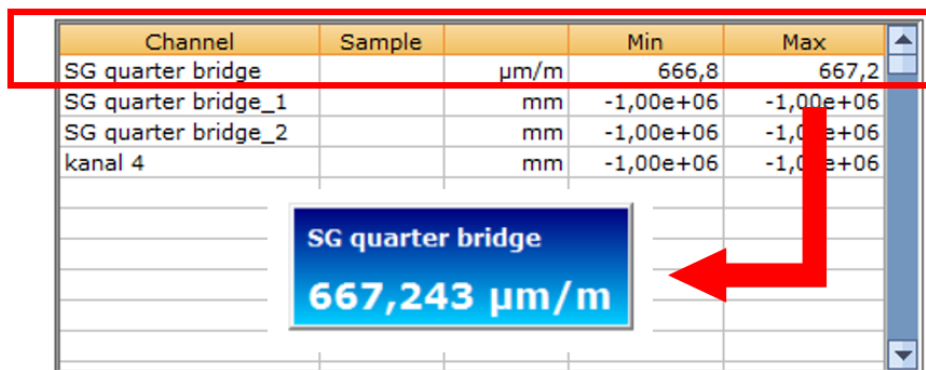


Figure 4.21. Strain gage quarter bridge showing the maximum and minimum strain values

Stress is calculated by the given formula below which is derived according to Theory of Simple Bending:

$$\sigma = \frac{6FL}{bh^2} \quad \text{Eqn 5}$$

In the literature, the elastic modulus of X70 steel is given as 210 GPa [33]. The calculated stresses according to the above formula (\*), strain measurements and the stress calculated with Hooke's law (\*\*) are given in Table 4.5.

Table 4.5. Stress values calculated according to the strain gage measurements and moment formulas

<i>Load (N)</i>	<i>Stress (MPa) *</i>	<i>Strain (<math>\mu\text{m/m}</math>)</i>	<i>Stress (MPa) **</i>
148	94.6	468.1	98.3
164	104.8	511.0	107.3
195	124.6	589.7	123.8
222	141.9	667.2	140.1
240	153.5	713.2	149.8
259	165.6	767.1	161.1

The stress values obtained from Hooke's law and the strain gage measurements are almost the same with the stress calculated according to the moment formula given above. This overlap shows that the formula used for stress calculation is correct. With the same approach, the below formula will be used for the hourglass type specimen:

$$\sigma = \frac{32FL}{\pi d^3} \quad \text{Eqn 6}$$

## 4.8 Fractographic Analysis

Fracture surfaces of different type of specimens subjected to rotating bending fatigue test were examined with visual inspection first and then detail analysis was performed with SEM. The fracture surfaces were analyzed from the point of morphology and fatigue failure features. In addition, striation spacing was used, in order to examine the crack growth behavior of each test groups. With this method striation width was measured at a certain point and then the distance between that point and crack initiation point was measured as shown in Fig. 4.22. Stress intensity factor was calculated according to the formula given in Section 2.3. Then crack growth rate ( $da/dN$ ) vs. stress intensity factor ( $\Delta K$ ) in log scale was plotted for base metal, weld and HAZ.

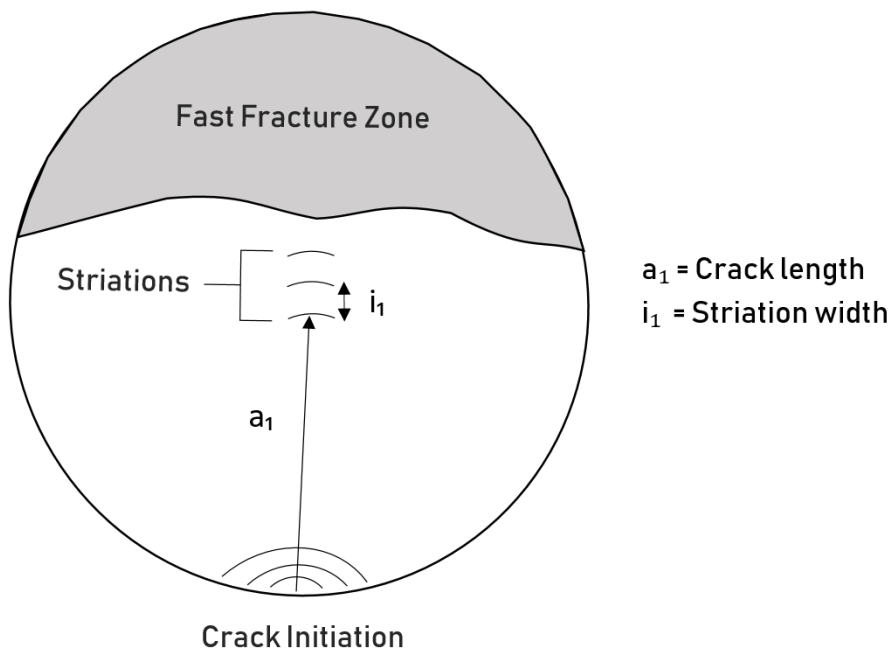


Figure 4.22. Striation width measurement

## CHAPTER 5

### RESULTS AND DISCUSSION

#### 5.1 Microstructural Analysis

The Figure 5.1 shows the microstructures of base metal in transverse and longitudinal directions at 1000X. The microstructure was determined to be uniform and fine acicular ferrite in transversal cut and rolling direction is clearly seen in longitudinal cut. When the optical micrographs in Fig. 5.2 were examined, it is clearly seen that grain size is the largest at the closest region to the weld section (HAZ1). Due to the growing grains in this region, larger, complex and amorph grain structure was observed. However, grain size of grain refined region (HAZ2) is very small compared to the coarse grained region (HAZ1) and the grains distributed homogeneously with equiaxed grain structures.

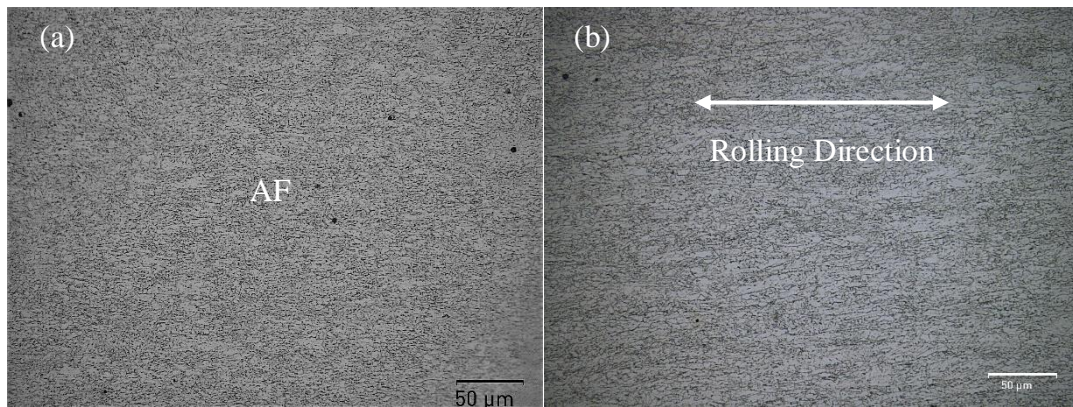


Figure 5.1. Optical micrographs of base metal region of X70 Steel (a) Transversal cut; AF (acicular ferrite) and (b) longitudinal cut at 1000X magnification

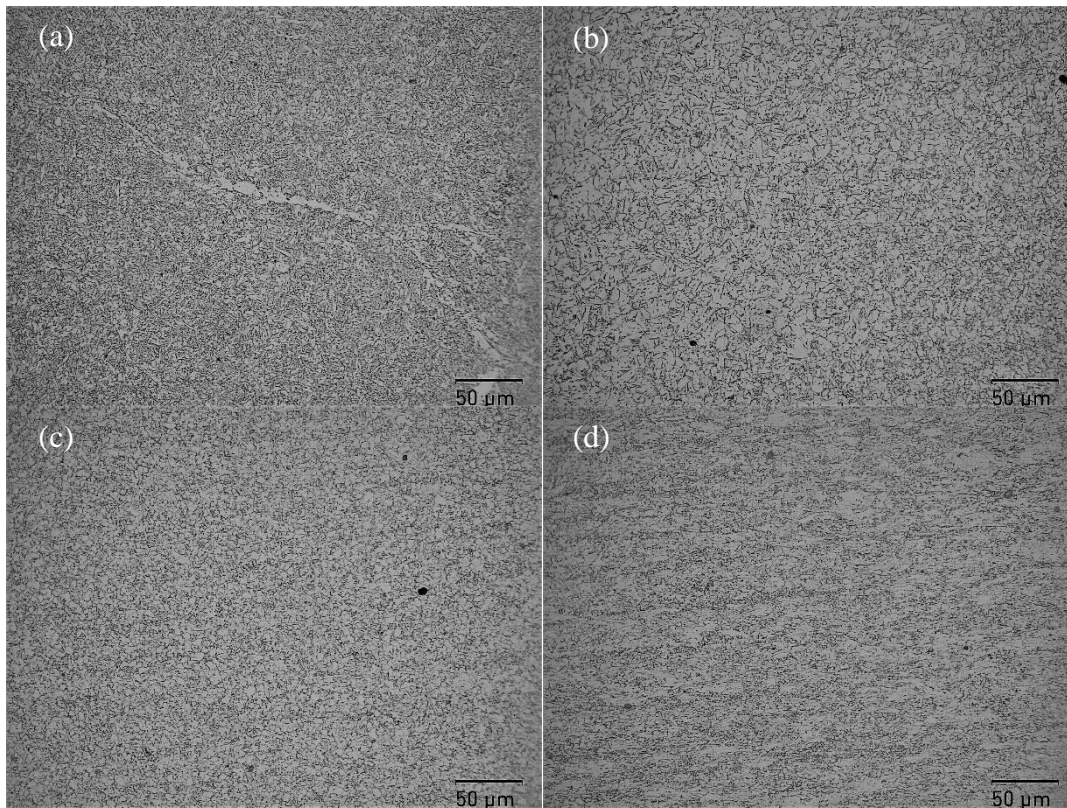


Figure 5.2. Optical micrographs of weld region and HAZ sub-regions; (a) weld metal, (b) HAZ1, (c) HAZ2, and (d) HAZ3 at 1000X magnification

In Fig. 5.3, the micrographs of sub-regions of HAZ in X70 steel obtained due to being affected from heat input at a different level during welding process and base metal are shown with using The Iron Carbon Phase Diagram.

The sample was also investigated with secondary electron imaging mode of SEM. Secondary electron images were taken from base metal and HAZ at different magnifications (Fig. 5.4). When the SE images are examined in Fig. 5.4, the region closest to the weld section (HAZ1) has the largest grain size. HAZ2 has smaller and coaxial grains as examined in optical micrographs. The grain sizes of HAZ3 are very close to the base metal's grain sizes. Secondary electron images were also taken from weld and the root of the weld region at the same magnifications (Fig. 5.5). In SE image of weld (Fig. 5.5 (a)), columnar grains and small ferrite grains between the columnar grain structures were observed.

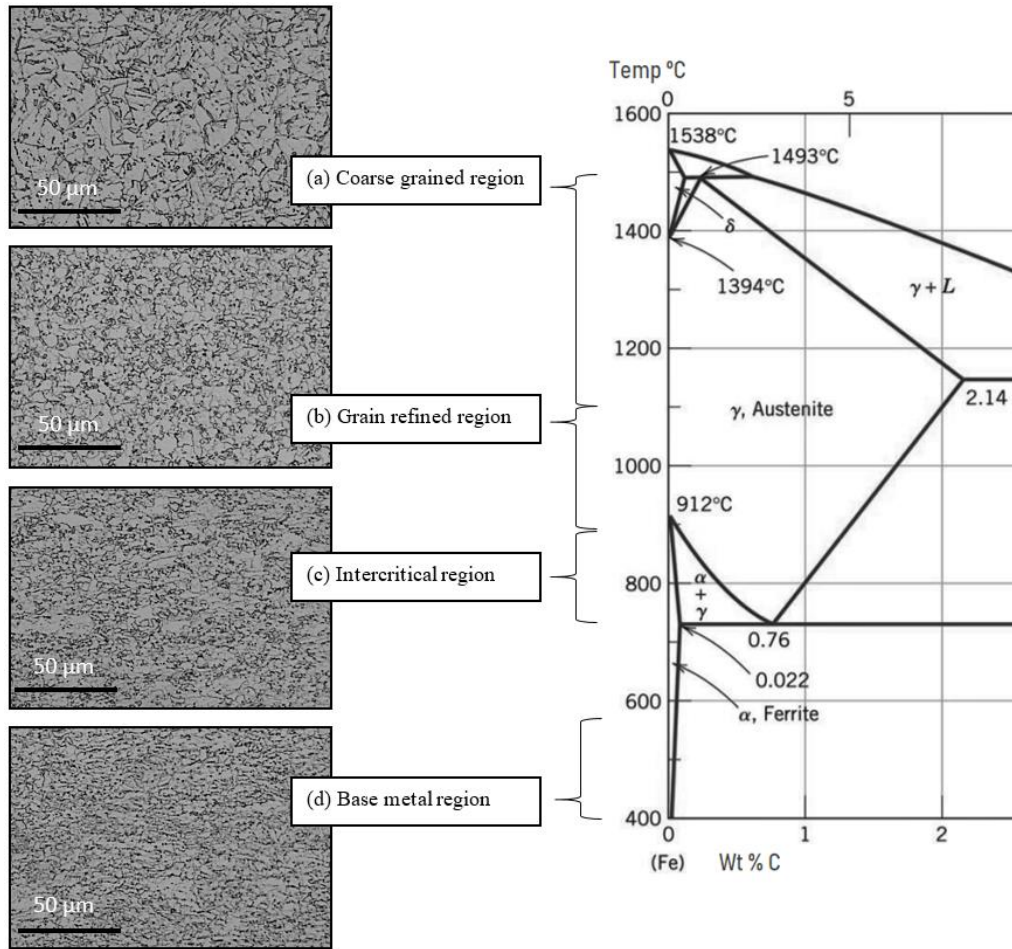
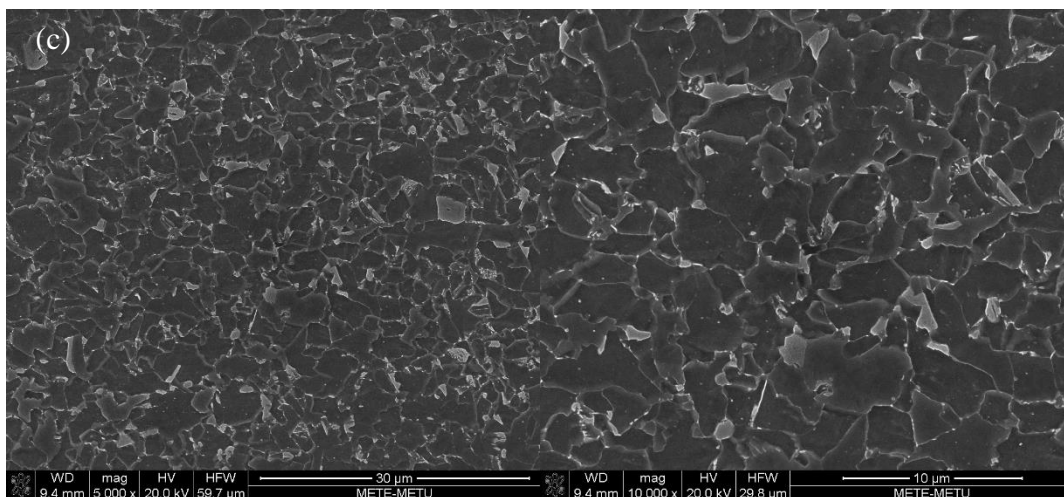
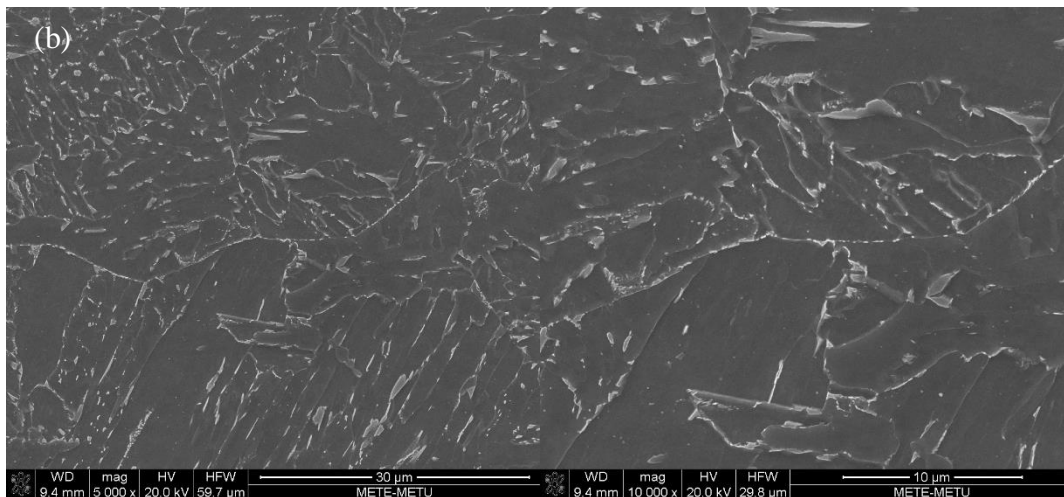
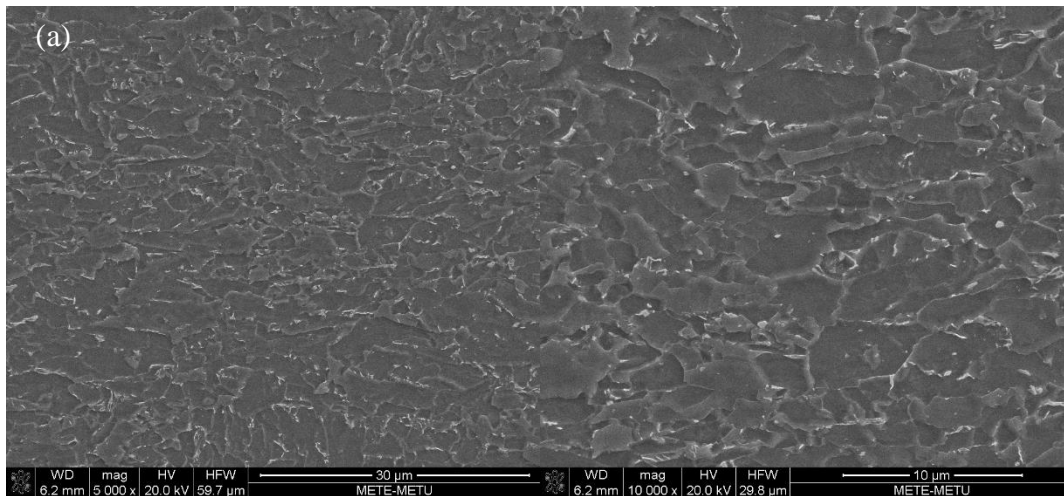


Figure 5.3. Sub-regions of HAZ in X70 Steel occurred due to heating during welding process; (a) coarse grained region (HAZ1), (b) grain refined region (HAZ2), (c) inter-critical region (HAZ3), (d) base metal region



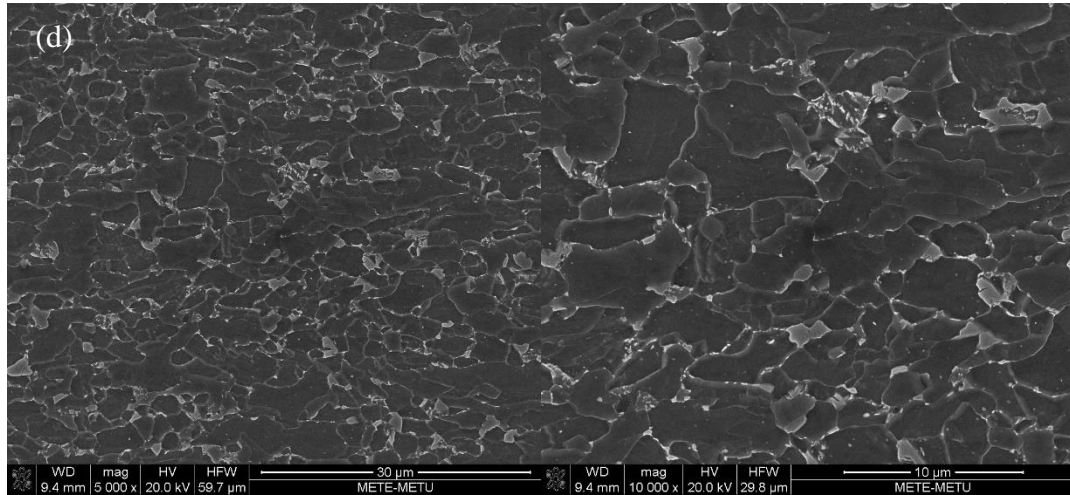


Figure 5.4. SE images from (a) base metal, (b) HAZ1, (c) HAZ2, and (d) HAZ3 of X70 Steel at 5000X and 10000X

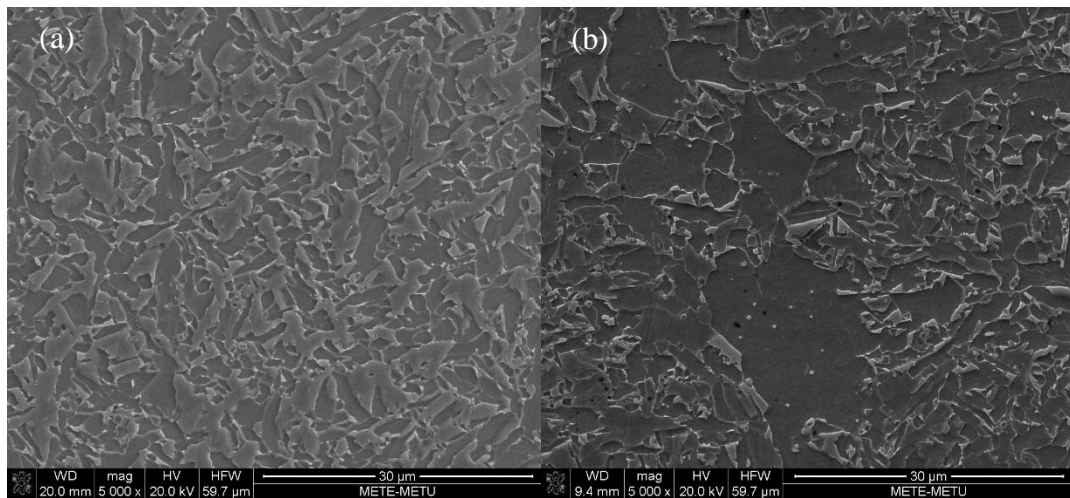


Figure 5.5. SE images from (a) weld zone and (b) root of weld zone at 5000X

## 5.2 Mechanical Analysis

In mechanical analysis section, tension, hardness and Charpy impact test results are given.

## 5.2.1 Tension Test Results

### 5.2.1.1 Base Metal

Fig. 5.6 and Table 5.1 shows the basic mechanical properties of the X70 Steel obtained from tensile tests. The average yield strength is 647 MPa and the average maximum tensile strength is 720 MPa. The results provide the tensile requirements for Grade X70 PSL 2 mentioned in Section 2.4. The axial strain was measured as 20 %. Fig. 5.7 shows the broken tensile test specimens of X70 Steel and the examination of the fracture surface of the specimens shows that fracture is ductile.

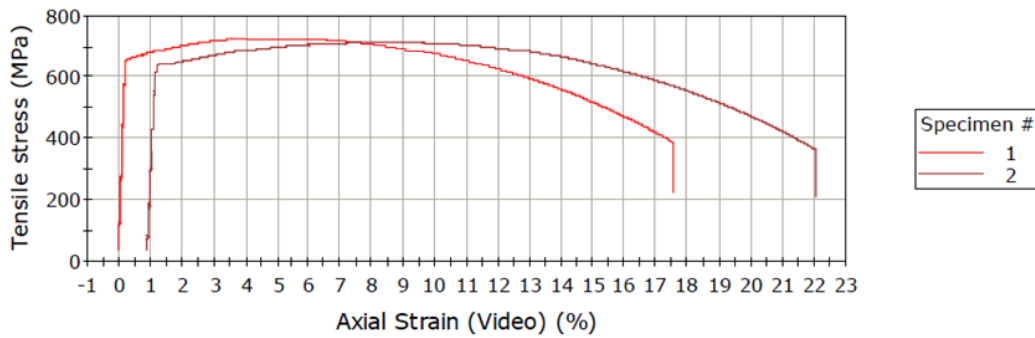


Figure 5.6. Stress – strain curves for specimens prepared from base metal region of X70 steel

Table 5.1. Tensile test results of specimens from base metal region of X70 steel

Specimen No	Maximum Tensile Stress (MPa)	Tensile Stress at Yield (Offset 0.2 %) (MPa)	Axial Strain at Break (%)
1	727	657	18
2	712	637	21
Average	720	647	20



Figure 5.7. Broken tensile test specimens prepared from base metal region of X70 steel

### 5.2.1.2 Weld Metal

Fig. 5.8 and Table 5.2 shows the mechanical properties of the weld zone specimens obtained from tensile tests. The average yield strength is 647 MPa and the average maximum tensile strength is 713 MPa. The axial strain was measured as 18 %. The results of the tensile tests showed that the yield strength, the ultimate tensile strength and the axial strain of weld metal were almost the same as the base metal. Fig. 5.9 shows the broken tensile test specimens prepared from weld zone of X70 Steel and the examination of the fracture surface of the specimens shows that fracture is ductile. The fracture was observed in the weld section of specimen 2 prepared in transverse direction and this result is proportional to the higher tensile strength of the base material than the weld metal.

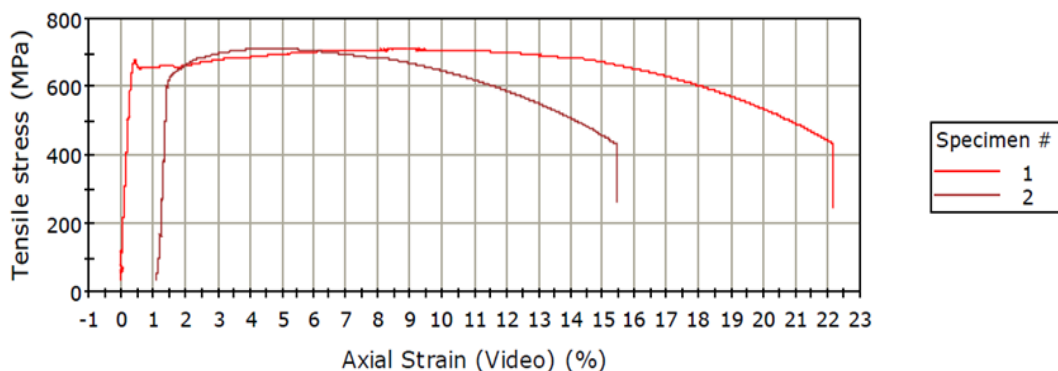


Figure 5.8. Stress – strain curves for specimens prepared from weld zone of X70 steel

Table 5.2. Tensile test results of specimens prepared from weld zone of X70 steel

Specimen No	Maximum Tensile Stress (MPa)	Tensile Stress at Yield (Offset 0.2 %) (MPa)	Axial Strain at Break (%)
1 (Longitudinal)	711	656	22
2 (Transversal)	714	638	14
Average	713	647	18

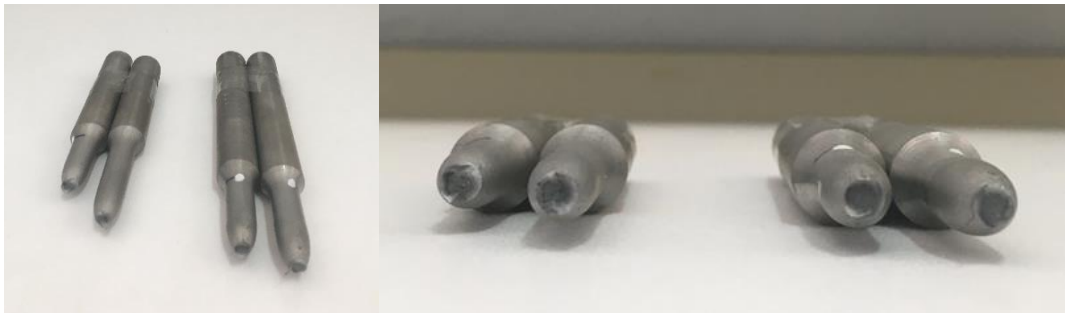


Figure 5.9. Broken tensile test specimens prepared from weld zone of X70 steel

### 5.2.2 Hardness Measurement Results

Table 5.3 shows the hardness measurements taken from three different lines, which are lower, mid, and upper lines.

Table 5.3. Hardness values of base metal, heat affected zone (HAZ1, HAZ2, and HAZ3) and weld

<b>Vickers Hardness Values (HV 0.5)</b>	<b>#</b>	<b>BM</b>	<b>HAZ3</b>	<b>HAZ2</b>	<b>HAZ1</b>	<b>WELD</b>
Lower line (left to right)	1	221	201	208	207	235
	2	235	213	195	202	221
	3	241	252	222	211	226
	4	210				206
	5	223				201
	6					208
Lower line (right to left)	1	219	225	205	207	
	2	227	229	190	201	
	3	232	232	199	199	
	4	211				
	5	215				
<b>Xm</b>		<b>223.4±10.3</b>	<b>225.3±17.4</b>	<b>203.2±11.3</b>	<b>204.5±4.5</b>	<b>216.2±13.2</b>
Midline (left to right)	1	208	228	208	198	221
	2	207	237	190	198	202
	3	205	235	205	193	203
	4	210				
	5	206				
Midline (right to left)	1	211	228	187	202	
	2	194	212	185	202	
	3	200	226	197	203	
	4	234				
	5	209				
<b>Xm</b>		<b>208.4±10.3</b>	<b>227.7±8.8</b>	<b>195.3±9.6</b>	<b>199.3±3.8</b>	<b>208.7±10.7</b>
Upper line (left to right)	1	211	241	206	219	207
	2	205	233	205	214	206
	3	216	204	201	202	213
	4	220	205			
	5	221				
Upper line (right to left)	1	223	196	195	209	
	2	236	208	198	202	
	3	217	188	192	205	
	4	220				
	5	217				
<b>Xm</b>		<b>218.6±8.0</b>	<b>210.7±19.3</b>	<b>199.5±5.5</b>	<b>208.5±6.9</b>	<b>208.7±3.8</b>

$X_m = \Sigma \text{hardness values} / \# \text{ of data}$

Standard Deviation:  $\sigma = \frac{1}{n-1} [\sum_{i=1}^n (X_i - X_m)^2]^{1/2}$  Eqn 7

In Fig. 5.10, the average hardness values are shown for the lines separately while Fig. 5.11 shows the hardness profiles for midline and the average of lower and upper lines. The reason of taking average of upper and lower lines are the similarity between cooling rates and expected hardness profiles. In Fig. 5.10, it is seen that inter-critical region (HAZ3) has the highest hardness value whereas the grain refined region (HAZ2) has the lowest hardness value. For the upper line, the highest hardness value was observed in base metal whereas the grain refined region (HAZ2) has the lowest hardness value again. It is thought that the phases occur due to heating and cooling in the weld metal, residual stresses in the weld zone and the additional welding wire and powder combination cause higher hardness values in the weld metal [7]. However, hardness values of the base metal are higher than the weld metal and they both have higher hardness values than HAZ2 and HAZ1. When Fig. 5.11 was examined, it is clearly seen that the average hardness values are higher than the midline's hardness values expect for HAZ3.

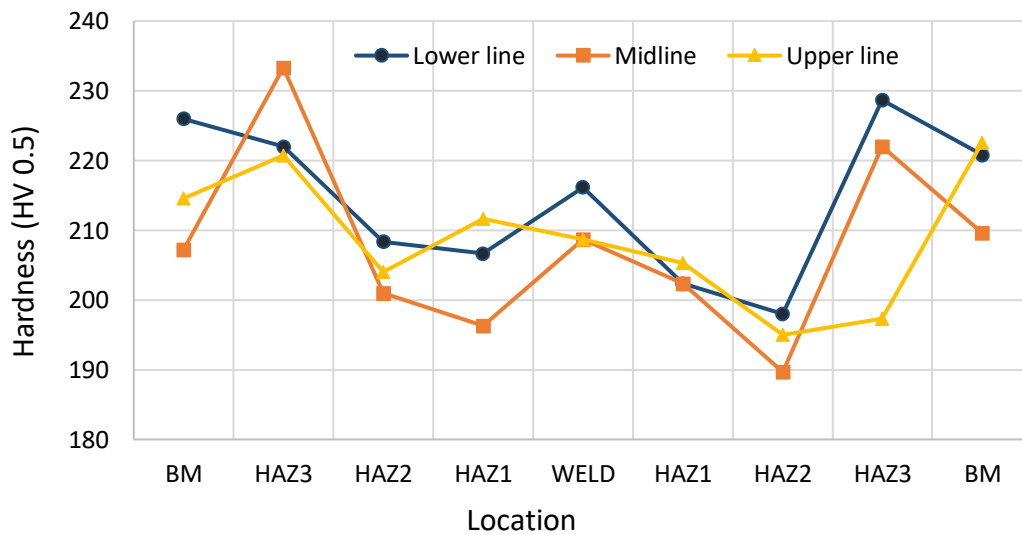


Figure 5.10. Hardness profiles of lower line, midline and upper line along the base metal, HAZ and weld

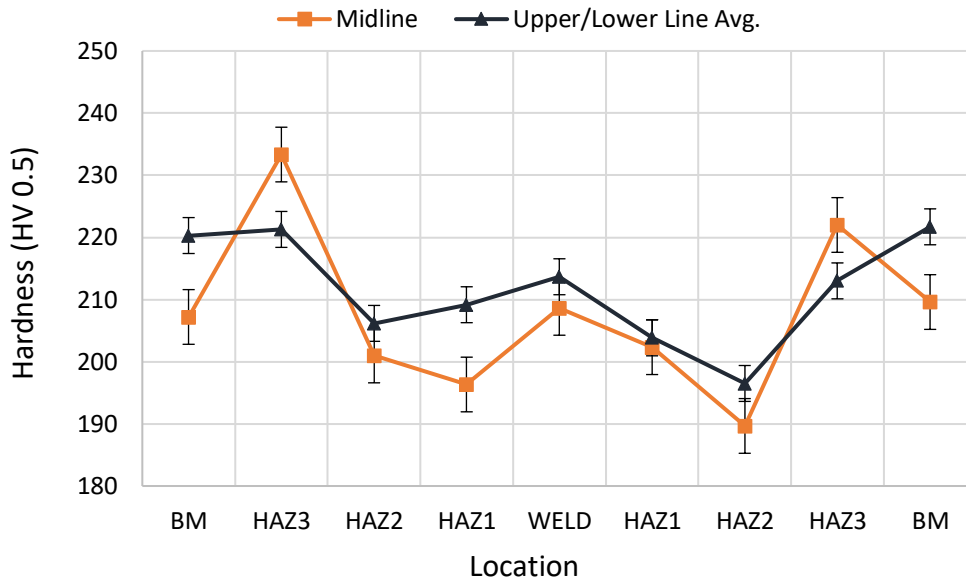


Figure 5.11. Hardness profiles of midline and upper/lower line avg. along the base metal (BM), HAZ and weld

### 5.2.3 Charpy Impact Test Results

Table 5.4 shows the Charpy impact test results at 25 and  $-30$  °C for base metal, fusion line 1 (FL1) and fusion line 2 (FL2) and weld metal. It is seen that Charpy impact energies of heat affected zone (FL1 and FL2) and weld metal decreased noticeably when the test temperature decreased from 25 °C to  $-30$  °C. However, very slight decrease was observed for the base metal as the temperature decreased. Base metal has the highest toughness of all regions for both test temperatures. The reason for base metal having better toughness is fine microstructure obtained due to TMCP. The reason for weld having the worst toughness could be the columnar coarse grains and inhomogeneous microstructure in weld region.

The test results at 25 °C shows that, the lowest impact energies observed in weld metal, fusion line 1, fusion line 2, and base metal respectively. For  $-30$  °C, fusion line 2 and weld zone have almost the same impact energy while fusion line 1 has higher impact energy than they have. According to the ASTM A370 Standard, the minimum impact energy that API 5L X70 Steel should have is 60 J at  $-15$  °C [7].

The test results show that the weld metal and the HAZ region have higher impact energies than 60 J even at  $-30\text{ }^{\circ}\text{C}$ .

Table 5.4. Charpy impact test results at 25 and  $-30\text{ }^{\circ}\text{C}$  for BM, fusion line 1, fusion line 2, and weld

Sample	No	Impact Energy (J) for $25\text{ }^{\circ}\text{C}$	Fracture Behavior at $25\text{ }^{\circ}\text{C}$	Impact Energy (J) for $-30\text{ }^{\circ}\text{C}$	Fracture Behavior at $-30\text{ }^{\circ}\text{C}$
Base Metal	1	335	100 % Ductile	282	100 % Ductile
	2	312	100 % Ductile	315	100 % Ductile
	3	335	100 % Ductile	308	100 % Ductile
	<b>X<sub>m</sub></b>	<b>327 ± 13</b>		<b>302 ± 17</b>	
Fusion Line 1	1	163	82 % Ductile	124	67 % Brittle
	2	186	92 % Ductile	63	100 % Brittle
	3	150	86 % Ductile	80	100 % Brittle
	<b>X<sub>m</sub></b>	<b>166 ± 18</b>		<b>89 ± 31</b>	
Fusion Line 2	1	210	100 % Ductile	60	100 % Brittle
	2	207	100 % Ductile	59	100 % Brittle
	3	121	52 % Ductile	77	89 % Brittle
	<b>X<sub>m</sub></b>	<b>179 ± 51</b>		<b>65 ± 10</b>	
Weld	1	143	92 % Ductile	56	100 % Brittle
	2	168	100 % Ductile	60	100 % Brittle
	3	143	100 % Ductile	76	49 % Brittle
	<b>X<sub>m</sub></b>	<b>151 ± 14</b>		<b>64 ± 11</b>	

Fracture surfaces were examined with visual inspection first and the type of fractures were determined. The broken specimens tested at  $25\text{ }^{\circ}\text{C}$  and the corresponding structures at the fracture surfaces were shown in Fig. 5.12. Then detail analysis was performed with SEM and dimples were observed for ductile type of fracture behavior while cleavage planes were observed for brittle type of fracture behavior (Fig. 5.13). For mix type of fracture behavior, both dimples and cleavage planes were observed as shown in Fig. 5.13.

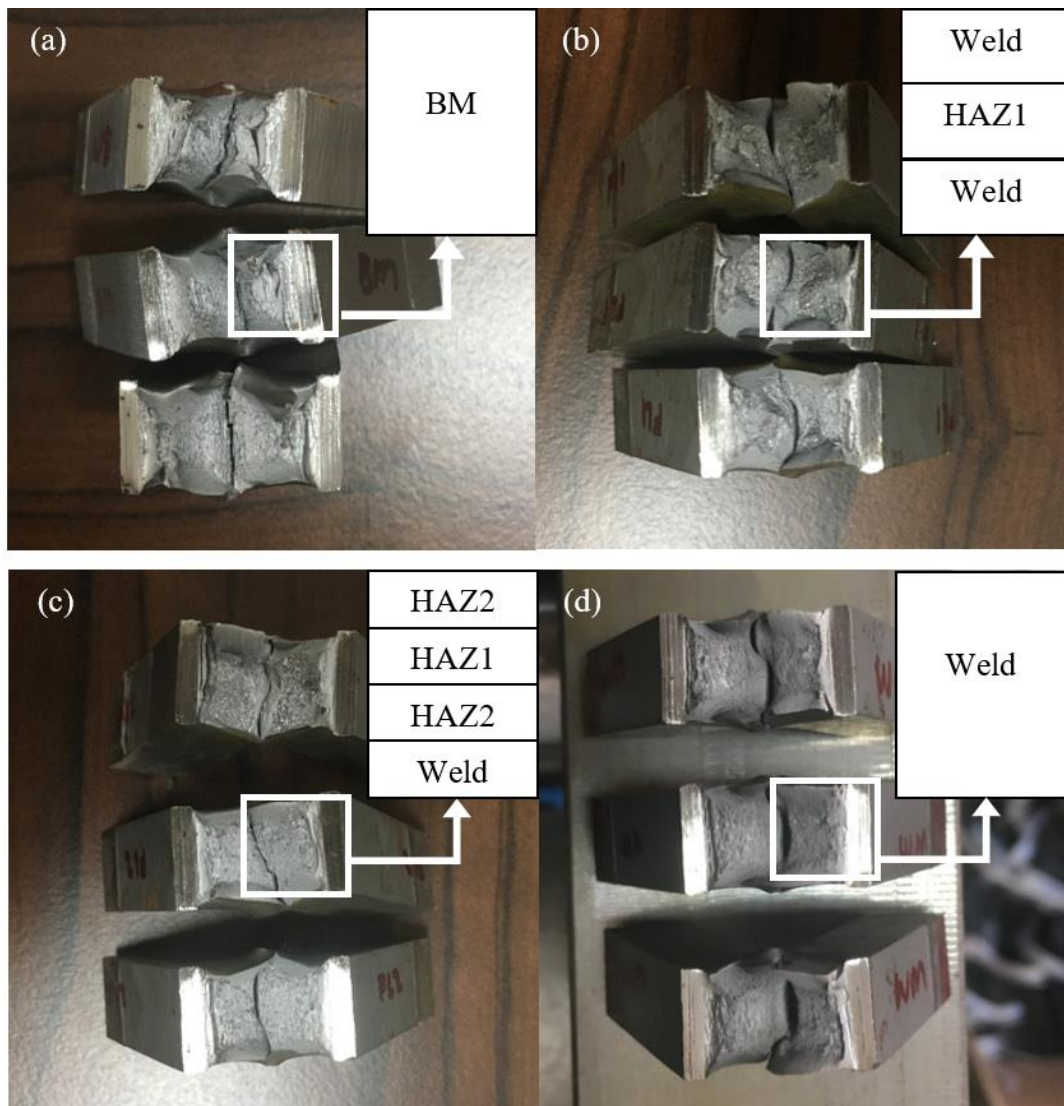


Figure 5.12. Impact specimens tested at 25 °C and the corresponding structures at the fracture surfaces; (a) base metal, (b) FL1, (c) FL2, and (d) weld metal

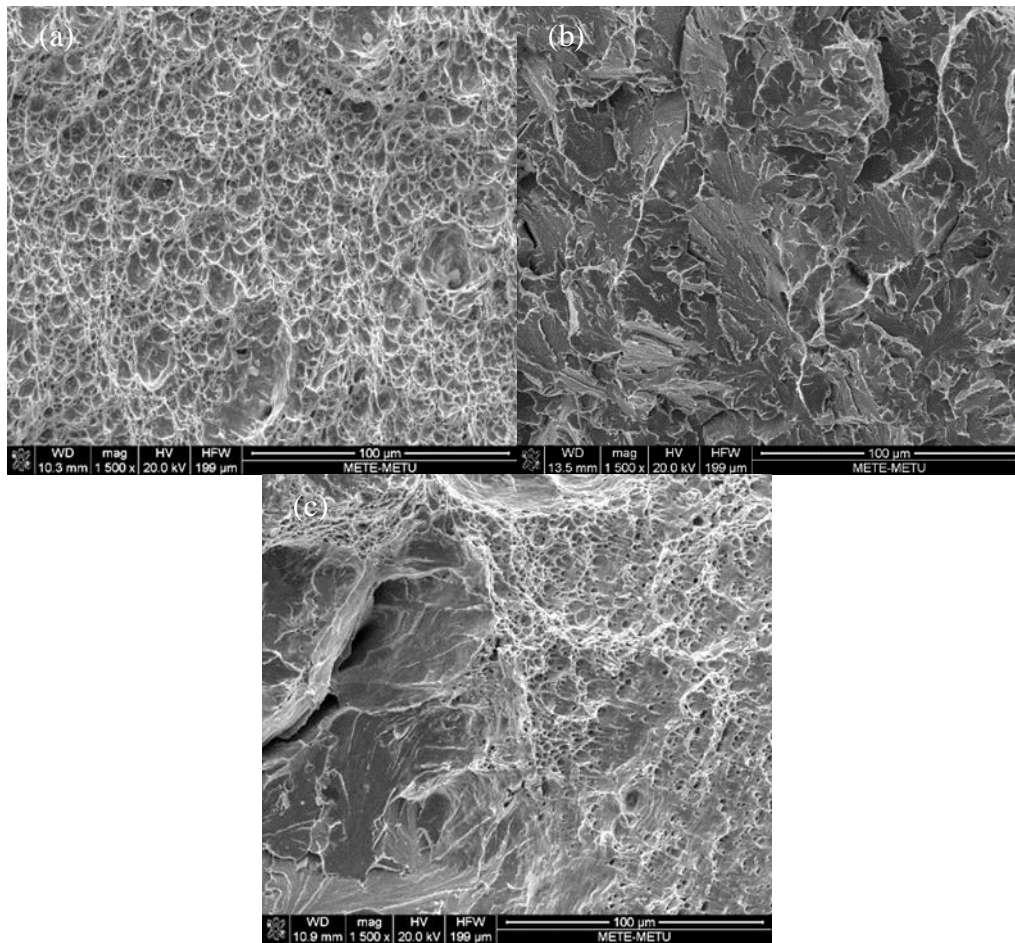


Figure 5.13. SEM images taken from FL2 tested at (a) 25 °C (No1), (b) - 30 °C, and (c) 25 °C (No3)

### 5.3 Rotating Bending Fatigue Test Results

Rotating Bending Fatigue Tests were conducted for X70 steel, weld and HAZ region at similar stress levels and the corresponding number of cycles (N) for failure were shown in Table 5.5. In order to plot realistic S-N curves, three tests were carried out for each stress level for at least five different stress values. Stress values were calculated by using Equation 6 in Section 4.7. Run out stress values are in the rows highlighted in yellow in Table 5.5.

Table 5.5. Fatigue test results

Base Metal			Weld			HAZ		
UTS %	Stress (MPa)	Cycles (N)	UTS %	Stress (MPa)	Cycles (N)	UTS %	Stress (MPa)	Cycles (N)
59.86	430.80	44188	61.59	438.72	64958	60.30	433.97	90730
60.30	433.97	50212	61.59	438.72	73731	60.30	433.97	119649
60.08	432.39	62127	61.59	438.72	74986	60.30	433.97	121589
56.56	407.04	130208	57.143	407.04	81003	56.56	407.04	354389
56.56	407.04	373384	57.143	407.04	101916	56.56	407.04	392224
56.56	407.04	380218	57.143	407.04	143520	56.56	407.04	417439
51.05	367.40	502382	53.363	380.12	114843	52.82	380.12	301306
51.05	367.39	755345	53.141	378.54	214574	52.82	380.12	346344
51.26	368.92	398653	53.363	380.12	731542	52.82	380.12	409575
48.20	346.86	2239065	42.913	305.68	1477432	42.47	305.68	3871598
45.33	326.27	3745876	42.913	305.68	2395840	42.47	305.68	3897706
45.33	326.27	4625852	40.023	285.09	4790998	42.47	305.68	3995807
42.47	305.68	4876351	38.466	274.00	4844323	39.61	285.09	6533022
42.47	305.68	8345411	38.466	274.00	4178918	37.41	269.25	7474836
42.47	305.68	9865997	38.689	275.59	5323854	37.41	269.25	7705032
37.85	272.42	4300707	42.913	305.68	5664374	37.41	269.25	7523984
33.01	237.57	7975507						

Regression lines were drawn for fatigue test data for all test groups as shown in Fig. 5.14, 5.15 and 5.16. The data for regression lines do not include the run out stress values. Run out stress values are shown with arrows in S-N plots. Coefficient of determination ( $R^2$ ) values were calculated for the regression curves. Since  $R^2$  values are higher than 0.9 for base metal, weld and HAZ, it is clear that regression lines for S-N plot represent the data points.

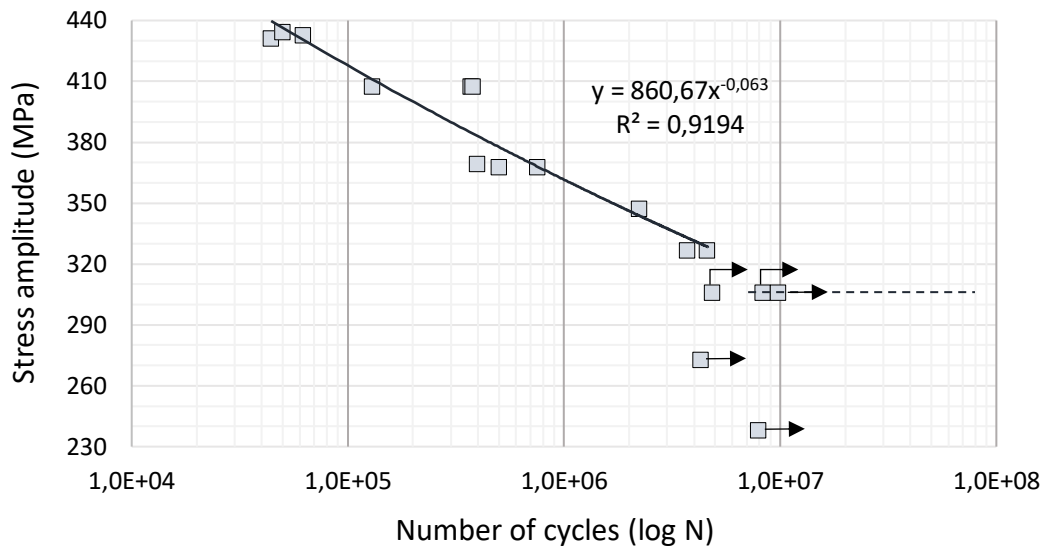


Figure 5.14. S-N plot for base metal

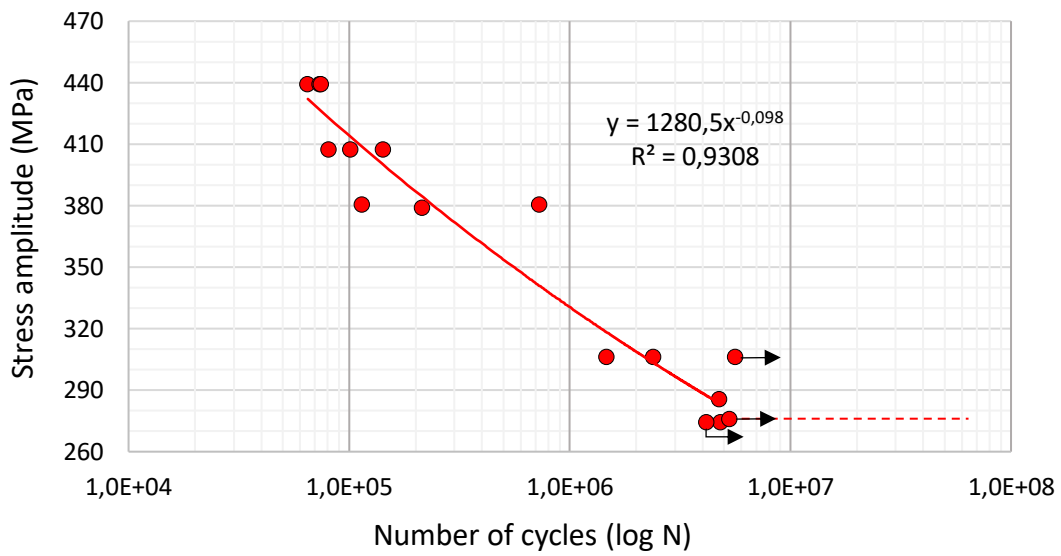


Figure 5.15. S-N plot for weld metal

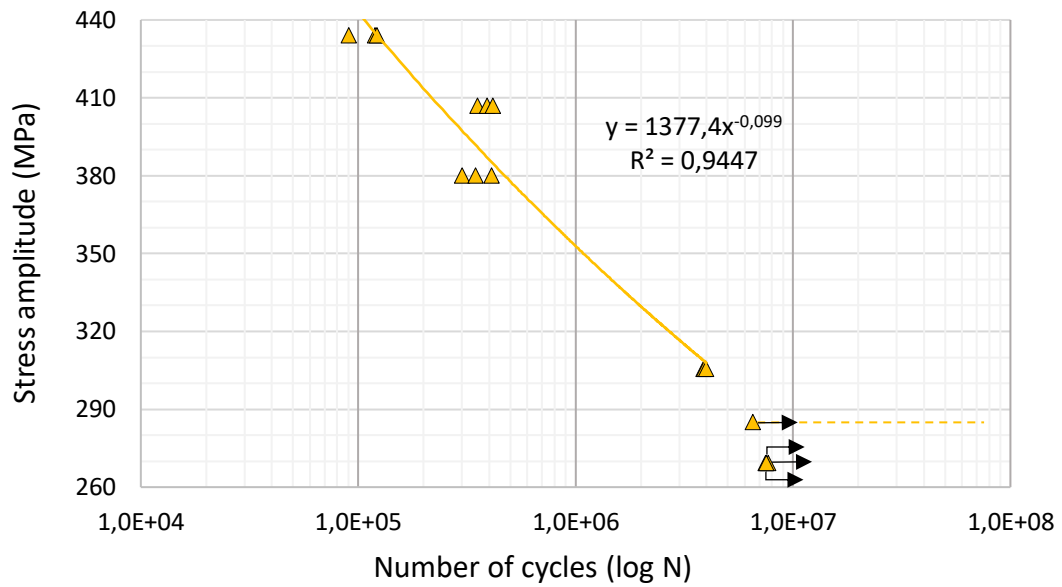


Figure 5.16. S-N plot for HAZ

The fatigue test data for all test groups are shown in Fig. 5.17. It is obviously seen that the fatigue life of weld at any stress level is lower than base metal and HAZ. The endurance limit of weld is also lower than base metal and HAZ. Surface irregularities and the possible defects in weld region could increase the crack susceptibility of weld and could lead to this result. When base metal and HAZ are compared, it is seen that at stress levels higher than approximately 380 MPa, HAZ has longer fatigue life. However, when the stress applied decreases below 380 MPa, the fatigue life of base metal is higher than HAZ's fatigue life. The endurance limit of base metal is higher than HAZ's endurance limit. This result is also seen in Fig. 5.18 where Fatigue ratios ( $\sigma_w/\sigma$ ) of base metal, weld and HAZ are compared. The fatigue ratios of all three test groups were found to be within the range specified for steels in Section 2.2.

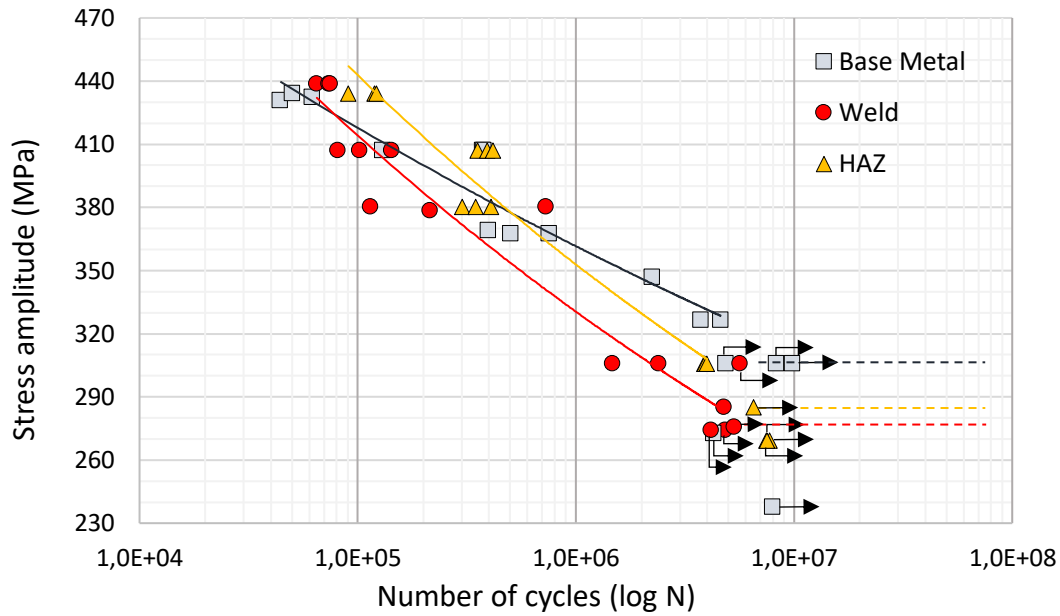


Figure 5.17. S-N curves for base metal, weld and HAZ

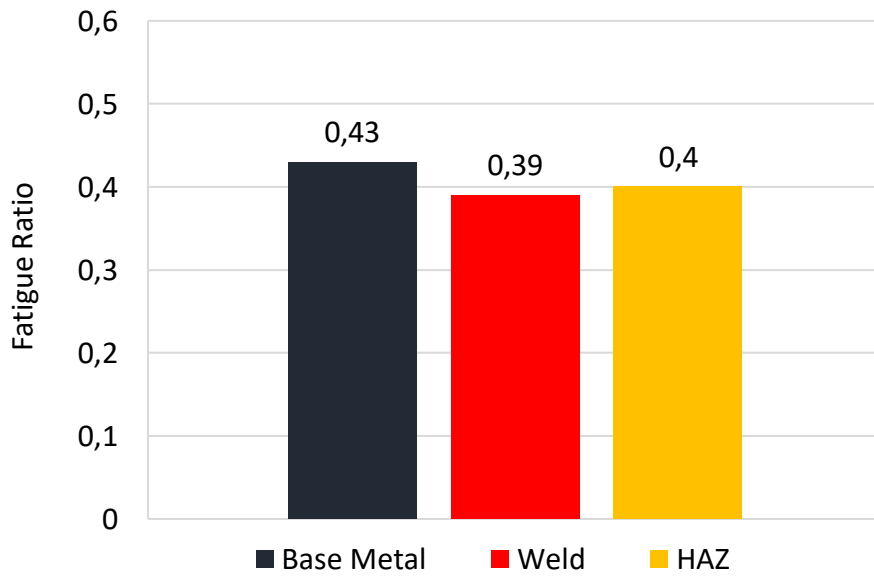


Figure 5.18. Fatigue ratios for base metal, weld and HAZ

Basquin slopes were also calculated by plotting S-N curves on a log-log scale as shown in Fig. 5.19.

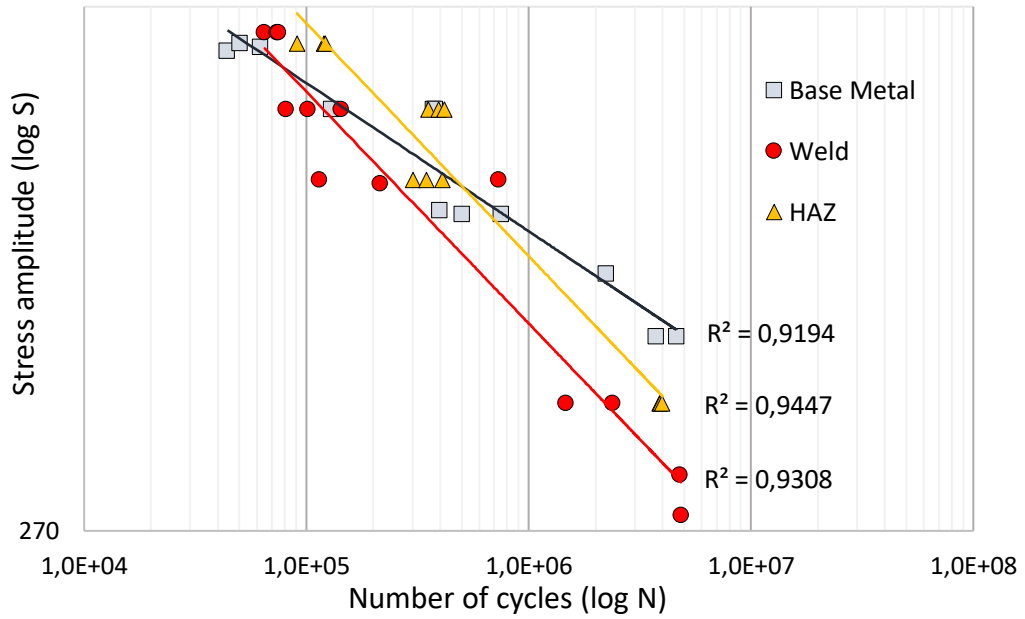
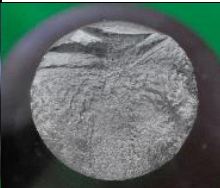
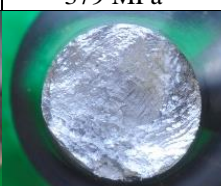
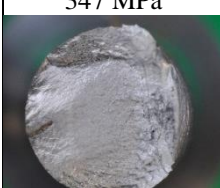


Figure 5.19. Basquin slopes for base metal, weld and HAZ

#### 5.4 Fractographic Analysis

Firstly, the fracture surfaces were analyzed by visual inspection from the point of morphology and fatigue failure features. Fracture surfaces of base metal, welded metal and HAZ subjected to different stress levels are shown in Table 5.6. At higher stress levels, multiple crack formation was observed for X70 steel and weld region while it was not observed in HAZ at any stress level (Table 5.6). The ratched markings, which are the indicators of multiple crack initiation and propagation were seen at the fracture surface of base metal failed at 434 MPa (Fig. 5.20 (a)). As a result of detailed examination of the sample with SEM in Fig. 5.20, dimples were observed indicating fast fracture zone and striations showing the crack propagation directions were found at different crack propagation regions.

Table 5.6. Macro fracture surfaces of all test groups subjected to rotating bending fatigue test

Base Metal	Weld	HAZ
434 MPa	439 MPa	434 MPa
		
407 MPa	407 MPa	407 MPa
		
369 MPa	379 MPa	380 MPa
		
347 MPa	306 MPa	306 MPa
		
	285 MPa	
		
	274 MPa	
		

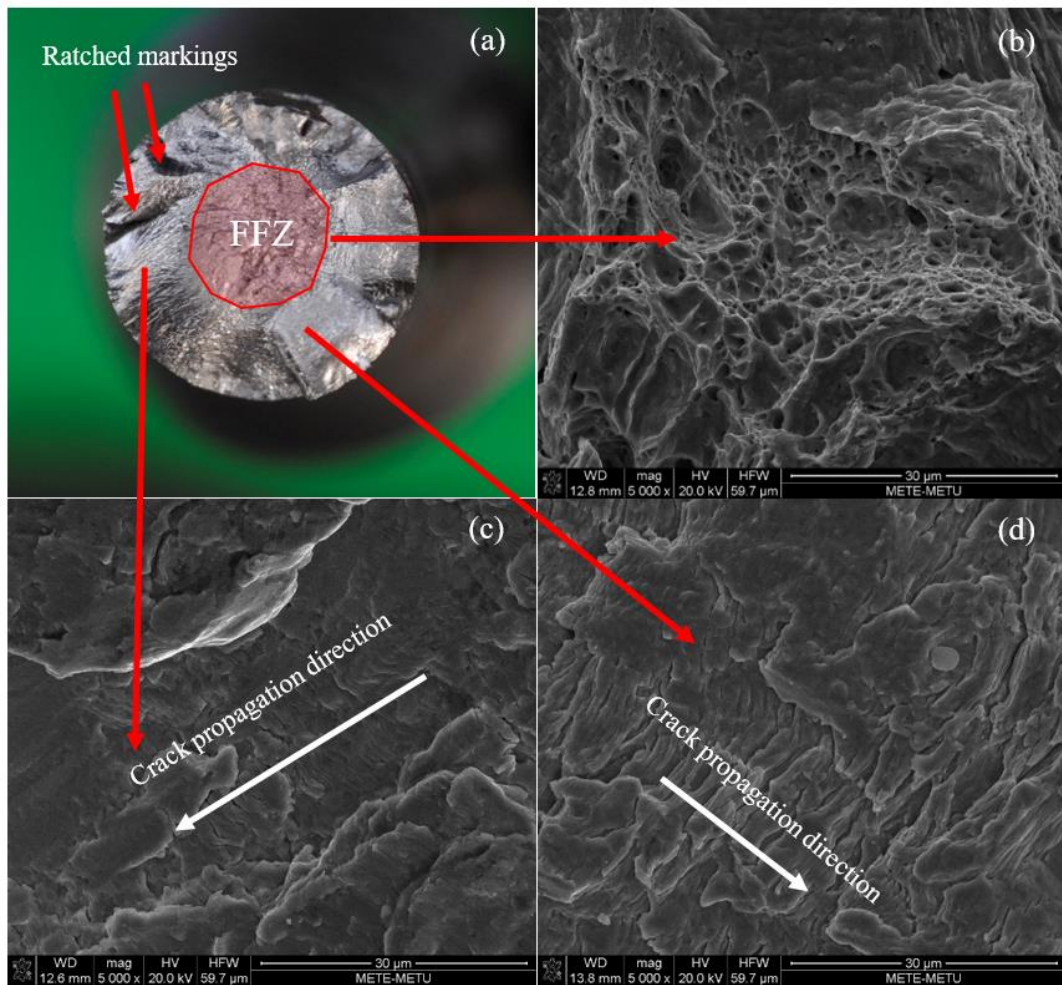


Figure 5.20. Fracture surface of base metal ( $\sigma = 434$  MPa); (a) ratched markings and FFZ (fast fracture zone), (b) dimples indicating rapid failure, and (c) and (d) striations indicating crack propagation direction

In most of the samples, smooth and burnished region was observed as a result of rubbing and an example of it is shown in Fig. 5.21 (a). When the sample (HAZ;  $\sigma = 380$  MPa) was examined with SEM in Fig. 5.21, tear ridge like patterns coalescing towards the crack propagation direction were observed at the center of the specimen and dimples indicating transgranular ductile fracture at FFZ (fast fracture zone) are shown.

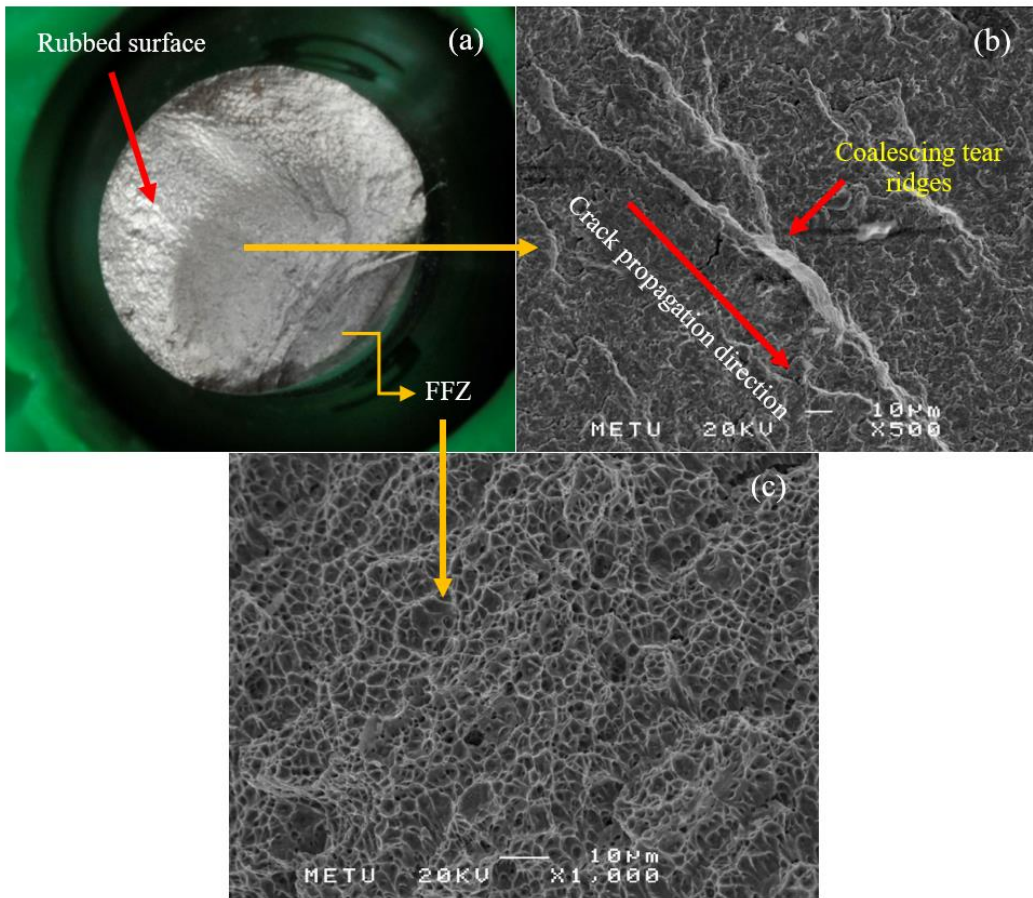


Figure 5.21. Fracture surface of HAZ ( $\sigma = 380$  MPa); (a) rubbed surface and FFZ (fast fracture zone), (b) tear ridge like patterns coalescing towards crack propagation direction, (c) dimples indicating rapid failure

Fig. 5.22 shows the welded specimen's fracture surface (failed at  $\sigma = 379$  MPa). Due to rubbing of bottom and top of the crack, the crack initiation site and a part of the crack propagation region seemed dark in SEM analysis and no findings were found. Dimples were observed in rapid failure region and tear ridge like patterns in the direction of crack propagation were shown.

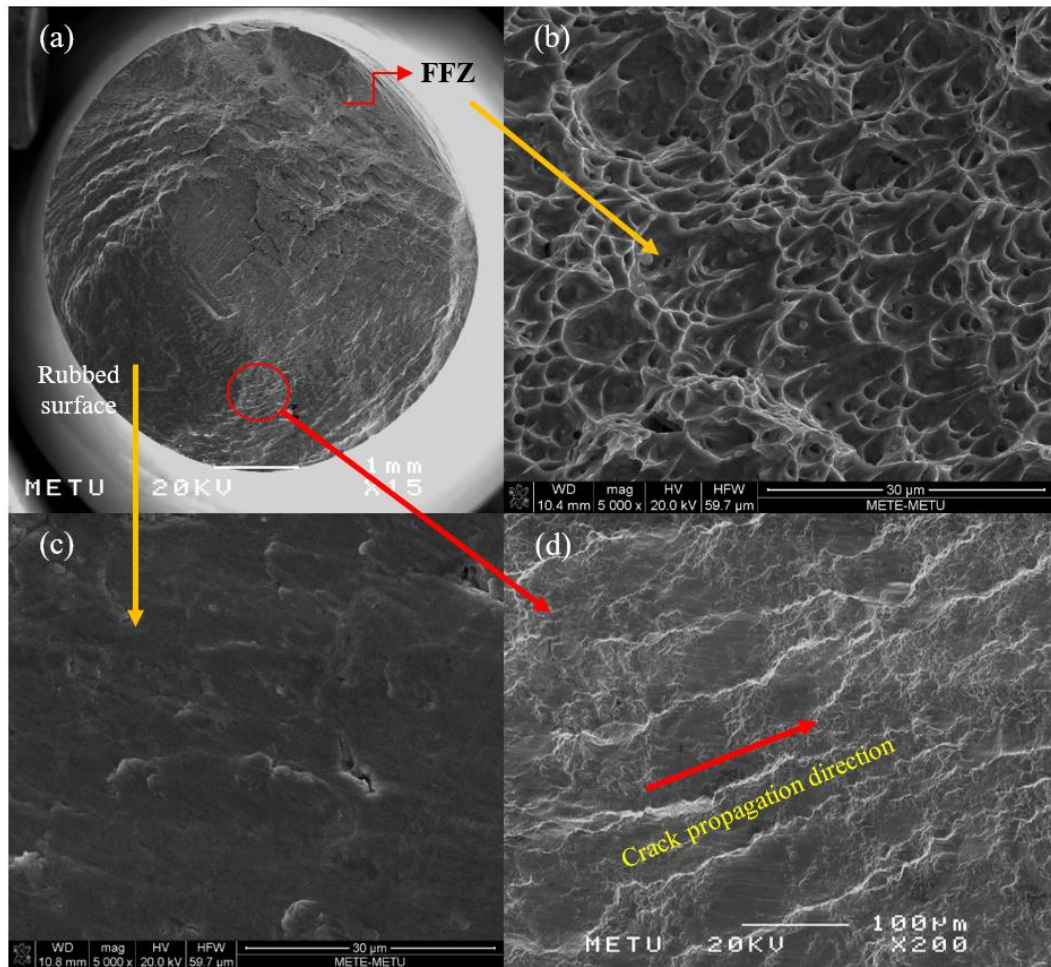


Figure 5.22. (a) Fracture surface of welded specimen (failed at  $\sigma = 379$  MPa), (b) dimples indicating rapid failure region, (c) rubbed surface, and (d) tear ridge like patterns showing the direction of crack propagation

#### 5.4.1 Striation Spacing

As it is mentioned in Section 2.3, striation spacing is a fractographic approach in order to reveal the crack growth behavior. Using striation spacing as shown in Fig. 23, 24 and 25, striation width was measured at a certain point and the distance between that point and the crack initiation point was measured. Crack initiation points were also shown in Figures. Striation width was measured more than one at the same region and the measured values were averaged in order to reach the nearest

correct result. Then the stress intensity factor ( $\Delta K$ ) was calculated by using the formulas for a surface crack in a solid cylinder stated in Section 2.3. The measured distances and the calculated values are shown in Table 5.7.

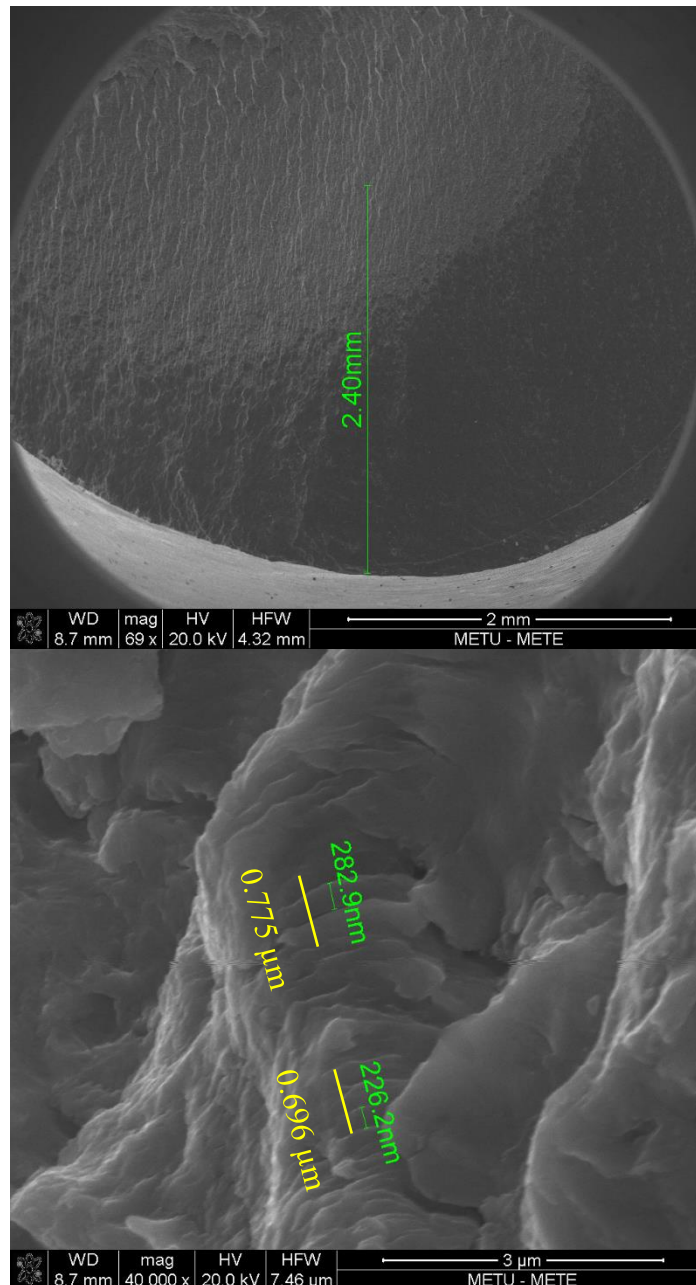


Figure 5.23. SEM images of base metal fracture surface; (a) striation measurement point, (b) striation width measurements

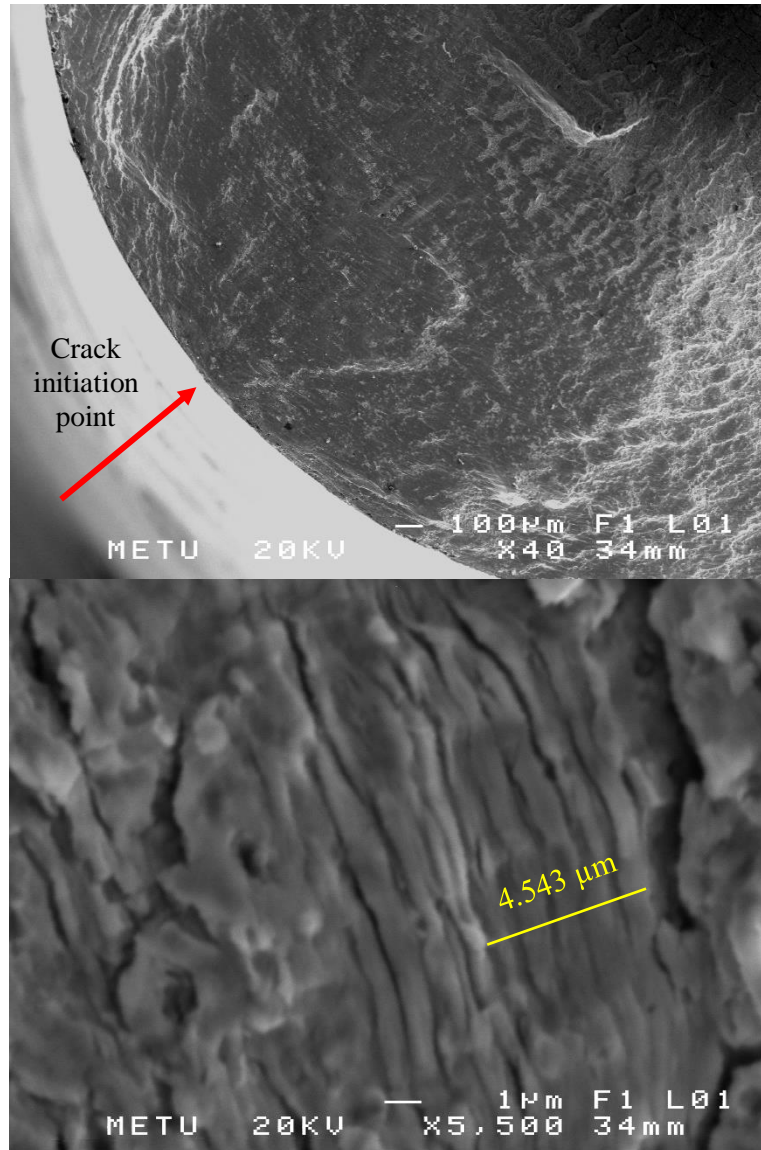


Figure 5.24. SEM images of welded metal fracture surface; (a) crack initiation point, (b) striation width measurement at 3.32 mm away from crack initiation point

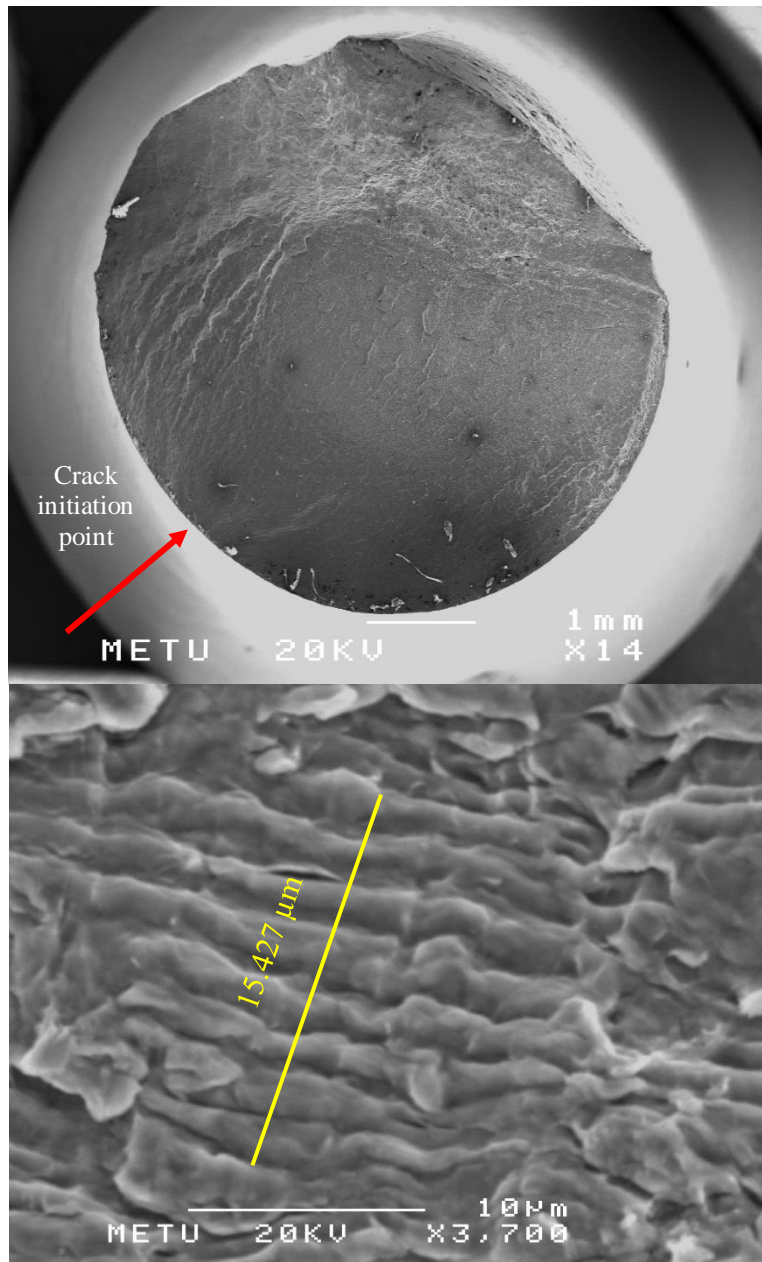


Figure 5.25. SEM images of HAZ fracture surface; (a) crack initiation point, (b) striation width measurement at 3.34 mm away from crack initiation point

Table 5.7. Data obtained from striation counting and stress intensity factor calculations

Specimen	Stress (MPa)	i (da/dN) ( $\mu\text{m}$ )	a (mm)	$\beta$	Y	G	F	$\Delta K$ ( $\text{MPa}\sqrt{\text{m}}$ )
Base metal	369	0.62	3.12	0.85	0.25	1.03	0.95	34.60
Base metal	407	0.38	2.87	0.78	0.30	0.93	0.86	33.19
Base metal	407	0.14	2.27	0.62	0.42	0.77	0.72	24.61
Base metal	407	0.25	2.40	0.65	0.39	0.80	0.74	26.17
Base metal	407	0.09	2.00	0.54	0.48	0.72	0.67	21.75
Weld	379	0.48	2.39	0.65	0.40	0.80	0.74	24.22
Weld	379	0.91	3.32	0.90	0.21	1.12	1.04	40.18
Weld	379	0.58	2.17	0.59	0.44	0.75	0.70	21.85
HAZ	434	0.94	1.96	0.54	0.49	0.72	0.67	23.03
HAZ	434	2.15	3.63	0.99	0.17	1.31	1.21	56.23
HAZ	407	1.93	3.34	0.91	0.21	1.13	1.04	43.53
HAZ	407	1.35	2.71	0.74	0.33	0.88	0.81	30.53

Bu using measured distances and calculations in Table 5.7, crack propagation rate (da/dN) versus stress intensity factor ( $\Delta K$ ) was plotted in log scale for all test groups (Fig. 5.27). The curves represent the region where Paris power law is valid [34]. Coefficient of determination ( $R^2$ ) values are 0.97 and 0.94 for HAZ and base metal, respectively, indicating the reliability of curve fitting. However, it is 0.81 for weld due to lack of striation spacing measurement data. As can be seen from Fig. 5.26, crack growth rate is lowest for base metal at same  $\Delta K$  value up to approximately 40  $\text{MPa}\sqrt{\text{m}}$ , showing that base metal has better performance than weld and HAZ. This result is also compatible with Charpy impact test results; the base metal having the highest toughness has higher resistance to crack propagation. The Paris slope (m) for base metal is 3.68, which is a reasonable value for a HSLA steel.

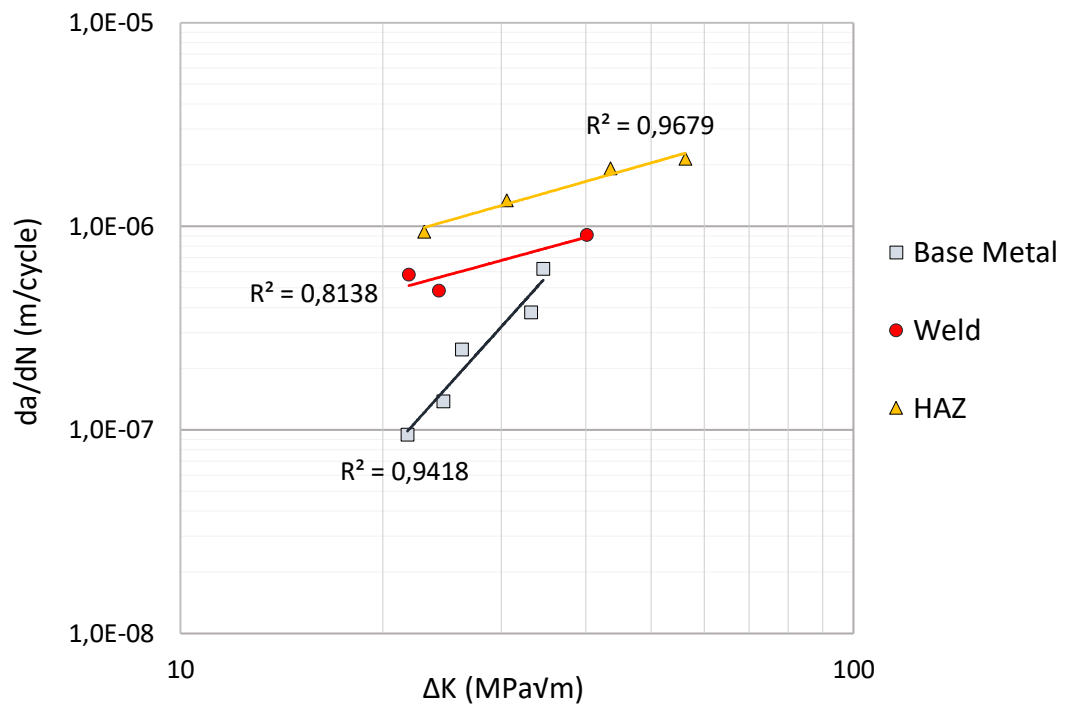


Figure 5.26. Crack growth behavior of base metal, weld and HAZ

## CHAPTER 6

### CONCLUSION

In this study, the fatigue behavior of base metal, weld and HAZ regions of welded API X70 pipeline steel was compared from the point of crack initiation and propagation. As a result of this study, the following results were achieved.

- Tensile properties of base metal and weld were found to be almost the same. Due to hardness measurements from base metal, weld and HAZ, very close values were obtained. Charpy impact test results show that base material has approximately twice impact energy than weld and HAZ at 25 °C. However, Charpy impact energies of HAZ and weld decreased noticeably at -30 °C while very slight decrease was observed for base metal. The reason for base metal having better toughness than weld and HAZ can be explained by fine and acicular ferrite microstructure obtained as a result of TMCP.
- The fatigue life of weld at any stress level is lower than base metal and HAZ, and this makes weld a potential region for possible crack initiation. This could be the result of surface irregularities and possible defects in weld region that increase the crack susceptibility of weld. At stress values applied below 380 MPa, base metal has better performance than HAZ. The fatigue ratios of all three test groups were found to be within the range specified for steels.
- Crack growth rate was found to be lowest for base metal at same  $\Delta K$  values up to approximately 40 MPa $\sqrt{m}$ . This result is also compatible with Charpy impact test results; the base metal having the highest toughness has higher resistance to crack propagation.
- The Paris slope (m) for base metal was found as 3.68 which is a reasonable value for a HSLA steel. This result support the idea that striation spacing can be used as a fractographic approach in order to estimate the crack growth behavior of materials.



## REFERENCES

- [1] M. Bilen, “Uygulanan Testler ve Mekanik Özelliklerinin İyileştirilmesi,” pp. 960–963, 2016.
- [2] L. B. Godefroid, L. C. Cândido, R. V. B. Toffolo, and L. H. S. Barbosa, “Microstructure and mechanical properties of two Api steels for iron ore pipelines,” *Mater. Res.*, vol. 17, pp. 114–120, 2014.
- [3] N. Engin and Z. Erman, “Düzce Üniversitesi Bilim ve Teknoloji Dergisi,” *Düzce Üniversitesi Bilim ve Teknol. Derg.*, vol. 4, no. Doğadan Esinlenen Optimizasyon Algoritmaları ve Optimizasyon Algoritmalarının Optimizasyonu, pp. 293–304, 2016.
- [4] S. Y. Shin, B. Hwang, S. Kim, and S. Lee, “Fracture toughness analysis in transition temperature region of API X70 pipeline steels,” *Mater. Sci. Eng. A*, vol. 429, no. 1–2, pp. 196–204, 2006.
- [5] L. Gajdoš, M. Šperl, and J. Bystrianský, “Fatigue behaviour of X70 steel in crude oil,” *Mater. Tehnol.*, vol. 49, no. 2, pp. 243–246, 2015.
- [6] J. Capelle, J. Gilgert, and G. Pluvinage, “Hydrogen Effect on Fatigue and Fracture of Pipe Steels.”
- [7] G. Üniversitesi Fen Bilimleri Dergisi, S. Aksöz, H. Ada, and A. Özer, “Toz Altı Ark Kaynak Yöntemiyle Üretilen API 5L X70 Kalite Çelik Boruların Mikroyapı ve Mekanik Özellikleri,” vol. 5, no. 1, pp. 55–64, 2017.
- [8] K. Miková, S. Bagherifard, O. Bokuvka, M. Guagliano, and L. Trško, “Fatigue behavior of X70 microalloyed steel after severe shot peening,” *Int. J. Fatigue*, vol. 55, pp. 33–42, 2013.
- [9] L. Ligang *et al.*, “Evaluation of the fracture toughness of X70 pipeline steel with ferrite-bainite microstructure,” *Mater. Sci. Eng. A*, vol. 688, no. January,

pp. 388–395, 2017.

- [10] J. V. S. J. S. P. J. K. J Billingham, “Review of the performance of high strength steels used offshore,” 2003.
- [11] S. APAY, M. GEL, and G. ÇİL, “Tozaltı Kaynak Yöntemi ile Farklı Kaynak Parametreleri Kullanılarak Birleştirilen API X70M PSL2 Malzemelerin Kaynak Bölgesinin İncelenmesi,” *Düzce Üniversitesi Bilim ve Teknol. Derg.*, vol. 6, no. 4, pp. 714–723, Aug. 2018.
- [12] Z. Tas, “Examination Of Mechanical Properties And Weld Zone Of X70 Pipe Steel After Welding,” *Int. J. Sci. Technol. Res.*, vol. 06, no. 07, pp. 148–152, 2017.
- [13] A. A. Akay, Y. Kaya, and N. Kahraman, “Tozaltı Ark Kaynak Yöntemi ile Birleştirilen X60, X65 ve X70 Çeliklerin Kaynak Bölgesinin Etüdü,” *Karaelmas Sci. Eng. J.*, vol. 3, no. 2, pp. 34–42, 2013.
- [14] P. Simion, V. Dia, B. Istrate, G. Hrituleac, I. Hrituleac, and C. Munteanu, “Study of fatigue behavior of longitudinal welded pipes,” *IOP Conf. Ser. Mater. Sci. Eng.*, vol. 145, no. 2, 2016.
- [15] E. Drexler and R. Amaro, “Fatigue Crack Growth Rates of API X70 Pipeline Steels in Pressurized Hydrogen Gas Compared with an X52 Pipeline in Hydrogen Service,” *Int. Hydrog. Conf. (IHC 2016) Mater. Perform. Hydrog. Environ.*, pp. 210–218, 2017.
- [16] W. D. Callister and D. G. Rethwisch, “Materials Science and Engineering 9th Edition,” *Comput. Sci. Eng.*, 2014.
- [17] K. Lieb, R. Horstman, B. Power, R. Meltzer, M. Vieth, and O. Vosikovsky, “Effects of Stress Ratio on Fatigue Crack Growth Rates in X70 Pipeline Steel in Air and Saltwater,” *J. Test. Eval.*, vol. 8, no. 2, p. 68, 1980.
- [18] H. E. Boyer and American Society for Metals., *Atlas of Fatigue Curves*. American Society for Metals, 1985.

- [19] Ü. B. Güleken, “Effect of Hydrogen on Fatigue Behavior of a Cadmium Coated High Strength Steel,” Middle East Technical University, 2019.
- [20] Ç. İlhan, “The Effects of chromic acid anodizing on fatigue behavior of (AMS4050) 7050 T7451 aluminum alloy,” Middle East Technical University, 2019.
- [21] P. C. Miedlar, A. P. Berens, A. Gunderson, and J. P. Gallagher, “DTDHandbook | Summary of Stress Intensity Factor Information | Selected Stress Intensity Factor Cases,” in *Damage Tolerant Design Handbook*, 2002.
- [22] American Petroleum Institute (API), “API Specification 5L, 46th Edition, Line Pipe,” 2018.
- [23] N. Shikanai, S. Mitao, and S. Endo, “Recent development in microstructural control technologies through the thermo-mechanical control process (TMCP) with JFE Steel’s high-performance plates,” *JFE Tech. Rep.*, vol. 11, no. 11, pp. 1–6, 2008.
- [24] U. TOSUN, “Investigating the Fracture Behaviour of X70M Linepipe Steel Girth Weldments via Single Edge Notched Tension and Bend Tests,” 2018.
- [25] M. C. Zhao, K. Yang, and Y. Shan, “The effects of thermo-mechanical control process on microstructures and mechanical properties of a commercial pipeline steel,” *Mater. Sci. Eng. A*, vol. 335, no. 1–2, pp. 14–20, Sep. 2002.
- [26] S. A. Atta-Agyemang, M. A. Kesse, P. Kah, and J. Martikainen, “Improvement of strength and toughness: The effect on the weldability of high-strength steels used in offshore structures,” *Proc. Inst. Mech. Eng. Part B J. Eng. Manuf.*, vol. 231, no. 3, pp. 369–376, 2017.
- [27] P. C. Sharma, *A textbook of production technology : manufacturing process*. S. Chand & Company, 2006.
- [28] K. Weman, *Welding Processes Handbook (Second edition)*. Woodhead Publishing, 2012.

- [29] W. Pang, “The structure and properties of the heat affected zone of structural plate steels welded by high productivity processes,” 1993.
- [30] S. M. Beden, “Environment Effects on Fatigue Crack Growth Rate in Api 5L X70 and X80 Steel Pipelines.”
- [31] N. Nanninga, A. Slifka, Y. Levy, and C. White, “A review of fatigue crack growth for pipeline steels exposed to hydrogen,” *J. Res. Natl. Inst. Stand. Technol.*, vol. 115, no. 6, pp. 437–452, 2010.
- [32] B. Peirson, “Comparison of the ASTM Comparative Chart Method and the Mean Line Intercept Method in Determining the Effect of Solidification Rate on the Yield Strength of AA5182,” pp. 1–15, 2005.
- [33] W. Zhao, T. Warren Liao, and L. Kompotiatis, “Stress and Springback Analyses of API X70 Pipeline Steel Under 3-Roller Bending via Finite Element Method,” *Acta Metall. Sin. (English Lett.)*, vol. 30, no. 5, pp. 470–482, May 2017.
- [34] E. Poursaeidi, M. Sanaieei, and H. Bakhtyari, “Life estimate of a compressor blade through fractography,” *Int. J. Eng. Trans. A Basics*, vol. 26, no. 4, pp. 393–400, 2013.